REPORT DOCUMENTATION PAGE

Form Approved OMB NO. 0704-0188

1. REPORT DATE (DD-MM-YYYY)	2. REPORT TYPE	3. DATES COVERED (From - To)
09-11-2017	Final Report	23-Jun-2014 - 22-Sep-2017

4. TITLE AND SUBTITLE
Final Report: Experimental investigation of the micromechanics of rock damage during dynamic loading events (ARO Research Area 2.1: Terrestrial Sciences)

5a. CONTRACT NUMBER
W911NF-14-1-0276

5b. GRANT NUMBER

5c. PROGRAM ELEMENT NUMBER
611102

6. AUTHORS

5d. PROJECT NUMBER

5e. TASK NUMBER

5f. WORK UNIT NUMBER

7. PERFORMING ORGANIZATION NAMES AND ADDRESSES
University of Texas at Arlington
701 South Nedderman Drive
Box 19145
Arlington, TX 76019 -0145

8. PERFORMING ORGANIZATION REPORT NUMBER

9. SPONSORING/MONITORING AGENCY NAME(S) AND ADDRESS (ES)
U.S. Army Research Office
P.O. Box 12211
Research Triangle Park, NC 27709-2211

10. SPONSOR/MONITOR'S ACRONYM(S)
ARO

11. SPONSOR/MONITOR'S REPORT NUMBER(S)
65447-EV-H.6

12. DISTRIBUTION AVAILIBILITY STATEMENT
Approved for public release; distribution is unlimited.

13. SUPPLEMENTARY NOTES
The views, opinions and/or findings contained in this report are those of the author(s) and should not contrued as an official Department of the Army position, policy or decision, unless so designated by other documentation.

14. ABSTRACT

15. SUBJECT TERMS

16. SECURITY CLASSIFICATION OF:			17. LIMITATION OF ABSTRACT	15. NUMBER OF PAGES	19a. NAME OF RESPONSIBLE PERSON
a. REPORT	b. ABSTRACT	c. THIS PAGE			William Griffith
UU	UU	UU	UU		19b. TELEPHONE NUMBER 817-272-9666

RPPR Final Report
as of 04-Sep-2018

Agency Code:

Proposal Number: 65447EVH **Agreement Number: W911NF-14-1-0276**
INVESTIGATOR(S):

Name: William A Griffith
Email: wagriff@uta.edu
Phone Number: 8172729666
Principal: Y

Organization: **University of Texas at Arlington**
Address: 701 South Nedderman Drive, Arlington, TX 760190145
Country: USA
DUNS Number: 064234610 EIN: 756000121
Report Date: 22-Dec-2017 Date Received: 09-Nov-2017
Final Report for Period Beginning 23-Jun-2014 and Ending 22-Sep-2017
Title: Experimental investigation of the micromechanics of rock damage during dynamic loading events (ARO Research Area 2.1: Terrestrial Sciences)
Begin Performance Period: 23-Jun-2014 **End Performance Period:** 22-Sep-2017
Report Term: 0-Other
Submitted By: William Griffith Email: griffith.233@osu.edu
Phone: (000) 000-0000
Distribution Statement: 1-Approved for public release; distribution is unlimited.

STEM Degrees: 1 **STEM Participants:** 2

Major Goals: The major goals of this project are stated below:
1: Conduct high strain rate compression tests of various rock types determine the dependence of compressive strength and damage on strain rate, peak stress and strain, and loading duration, with particular emphasis on isolating effects of mineralogy, grain size, and initial flaw distribution on failure properties at high strain rates.
2: Quantitative characterization of high strain rate brittle damage using Computed Tomography (CT) as well as optical and scanning electron microscopy.
3: Determination of the energy budget (including quantification of energy partitioned into creation of fracture surfaces in rocks) at high strain rates.
4: Evaluation/calibration of micromechanical models describing damage development acting across a spectrum of strain rates and stress states, from discrete fracture to pulverization.

Accomplishments: We have accomplished the first goal with an extensive suite of dynamic compression tasks. We have also accomplished goal 2, and the results are described in a recently published manuscript in Philosophical Transactions of the Royal Society A. The discussion below primarily addresses work we have done toward addressing Goals 3 and 4:

One proposed class of models that describe the pulverization process in rocks is based on an energy minimization principle, through which the balance of kinetic energy and surface energy creation involved in pulverization is such that the total energy is (e.g., Grady, 1982; Grady and Kipp, 1987; Key and Schultz, 2011). In these models, it is assumed that the fragment size produced during fragmentation (due to volumetric expansion) is governed by either by the conversion of kinetic energy into surface energy, or by the minimization of the total energy during fragmentation. In both scenarios, it is assumed that the dominant terms in the energy budget are kinetic energy and surface (fracture) energy. In addition to addressing the difference between compressive loading and tensile loading (as described in b. below), we have made major efforts to measure these energy terms:

i. Fracture surface energy: In our first manuscript resulting from this grant, we show that the energy dissipated in creation of new fracture surface area during a pulverization event in the laboratory can be up to 40% of the total dissipated energy. In this study our principal tool was Emmett-Brunauer-Teller (BET) analysis of specific surface area of our post-mortem rock fragments. This is much higher than generally accepted for earthquakes in the seismological community, but actually in line with recent work comparing the fracture energy computed from earthquake and rotary shear experiments (Nielsen et al., 2016). In that study, it was found that for small to medium earthquakes, fracture energies are equivalent, but for Mw>6-7 events, the fracture energy computed from

rotary shear experiments significantly underestimates the seismological fracture energy, and this difference can be accounted for by damage during natural earthquakes. This manuscript, Experimental constraints on dynamic pulverization as a dissipative process during seismic slip, has recently been accepted for publication in a special issue of the Royal Society of London publication Philosophical Transactions A.

ii. Kinetic energy: The second term, Kinetic Energy, is more elusive than surface energy, because it is transientand not preserved directly in the fragmented material. Furthermore, the majority of particles are too small to be tracked by high speed cameras. We have solved this problem by mapping ejected particles during fragmentation events on pressure sensitive thin films that line a steel ring surrounding the sample (see red strips in Figure 1) during a series of experiments (Figure 3). From the resulting pressure distributions, we can back out particle size and particle velocity distributions by considering the ejected particles as dynamic Hertzian spheres impacting a flat surface. We show in this analysis that the patterns of pressure distributions, and kinetic energy distributions, correspond very well with measured particle size distributions, and therefore are a good predictor of the fragmentation-pulverization transition, supporting the use of energy methods for relating particle sizes to strain rate conditions. That being said, a surprising result of the analysis suggests that the preserved kinetic energy is a very small portion (1-7%) of the dissipated energy. Given that fracture surface energy is on the order of 5-40% as discussed above, this suggest that either another major energy sink exists, or, the interpretation we prefer, is that a large percentage of kinetic energy is converted to frictional (heat) energy, highlighting a major difference between fragmentation under compressive and tensile loading. Results of this analysis are detailed in a manuscript “Energy Delocalization during Dynamic Rock Fragmentation”, which is now complete and will be submitted in the coming weeks.

b. Fragmentation under compressive vs. tensile loading

The fragmentation process may be fundamentally different under compression than tension. Given the well-known fact that rocks are an order of magnitude stronger under compression than tension, this is perhaps not very surprising, but as pointed out recently by Xu and Ben-Zion in their 2017 paper “Theoretical constraints on dynamic pulverization of fault zone rocks” published in Geophysical Journal International, the difference between these two processes can have major implications for understanding the occurrence of pulverized rocks along major faults. They argue that rock fragmentation/pulverization under isotropic tension could solve many of the scaling challenges between experimental pulverization and the natural prototype, most notably the fact that stress and strain rate thresholds for pulverization of rocks is too high to be achieved 10s of meters from fault zones.

In response to this challenge, we have designed a novel modification of the SHPB apparatus that allows us to study rock fragmentation under isotropic tension. The concept is motivated by the mechanics of fracture in mechanical stratigtraphy. The traditional homogeneous cylindrical specimen is replaced by a disk-shaped rock specimen sandwiched between two more compliant – but less compressible – disks (Figure 4). In our implementation, the inner disk is Westerly Granite and the outer disks are of lead. The lead disks are bonded to the inner granite disk, and when they are shortened axially by the incident bar compression wave induced by the striker bar, they expand radially at a faster rate than the granite, inducing an isotropic radial tension in the Westerly Granite at axial compression far below the uniaxial compressive strength of the granite. We instrument the Westerly Granite disk directly in addition to the incident and transmission bars, and we can back out the radial stress and strain rate within the granite disk. Remarkably, the disk fragments at much lower strain rates than under compression, and the fragment sizes correspond very closely to fragment sizes predicted by the energy-based models discussed above. We expect that this project will present a transformative advance in the way that we interpret pulverized rocks and will represent the “missing piece” in the puzzle of how – and under what circumstances – pulverized fault zone rocks form in nature.

After our initial proof of concept we are conducting further experiments to study this phenomenon, and pending sufficient progress, we should have a manuscript developed by the end of the summer and we will present our results at the 2017 AGU meeting in New Orleans.

Training Opportunities: Hamed Ghaffari was supported as a postdoctoral researcher for 2 years and three months of the project peiod. In May 2017 he left to assume a position he accepted as a postdoctoral researcher at the Massachusetts institute of Technology. This is a very good move for him professionally, and the opportunity came in large part based on the work he was conducting under this project. Hamed has two first authored manuscripts that we are still finishing that describe work done under this project, and they will be submitted within the coming months.

Troy Barber completed his MS degree during the reporting period (December 2016). The bulk of his salary support came from an NSF Graduate Research Fellowship, but he contributed substantially to accomplishing the major goals of this project, particularly goals 1-3:
1: Conduct high strain rate compression tests of various rock types determine the dependence of compressive strength and damage on strain rate, peak stress and strain, and loading duration, with particular emphasis on isolating effects of mineralogy, grain size, and initial flaw distribution on failure properties at high strain rates.
2: Quantitative characterization of high strain rate brittle damage using Computed Tomography (CT) as well as optical and scanning electron microscopy.
3: Determination of the energy budget (including quantification of energy partitioned into creation of fracture surfaces in rocks) at high strain rates.

In his MS work, Troy conducted high strain rate compression experiments on Arkansas Novaculite and Westerly Granite, and quantitatively characterized the fracture surface area - and implications for the energy budget - using Brunauer-Emmett-Teller and Scanning Electron Microscopic analysis. His results were published in Philosophical Transactions of the Royal Society A. He has also been working on characterizing fracture networks that develop during high strain rate rock failure by examining pre-failure specimens using MicroCT scanning techniques. This is the first project for his PhD project.

RPPR Final Report
as of 04-Sep-2018

Results Dissemination: a. Papers published in peer-reviewed journals

1. H.O. Ghaffari, W.A. Griffith, P. Benson, K. Xia, and R.P. Young, 2016, Observation of the Kibble-Zurek mechanism in microscopic acoustic crackling noises, Nature's Scientific Reports, doi:10.1038/srep21210.
2. Barber, Troy J. and W.A. Griffith, 2017, Experimental constraints on dynamic pulverization as a dissipative process during seismic slip, Philosophical Transactions of the Royal Society A, 375: 20160002. http://dx.doi.org/10.1098/rsta.2016.0002.
3. Ghaffari, H.O., W.A. Griffith, and P. Benson, 2017, Microscopic evolution of volcanic hybrid laboratory earthquakes, Nature Scientific Reports, 7, 40560, doi: 10.1038/srep40560

b. Papers published in non-peer-reviewed journals

-N/A

c. Presentations:

1. H.O. Ghaffari, W.A. Griffith, P. Benson, M.H.B. Nasseri, and R.P. Young, An artificial Ising system with collective phononic excitations, American Physical Society Meeting, March 14-18, Baltimore, MD.
2. Barber, T.J., H.O. Ghaffari, and W.A. Griffith, Controls on the formation of pulverized off-fault rocks: Laboratory investigations using Arkansas Novaculite, American Geophysical Union Fall Meeting, San Francisco, 2015 (Outstanding Student Paper Award Winner)
3. Ghaffari, H.O., T.J. Barber*, and W.A. Griffith, Dynamics of Fragmentation: Developing a non-EquilibriumMechanism for Impact-loading Tests on Rock Materials, American Geophysical Union Fall Meeting, San Francisco, 2015
4. Griffith, W.A., H.O. Ghaffari, T.J. Barber, and C.N. Borjas, INVITED, New perspectives on the transitionbetween discrete fracture, fragmentation, and pulverization during brittle failure of rocks, American Geophysical Union Fall Meeting, San Francisco, 2015
5 T. Barber, W.A. Griffith, Experimental constraints on dynamic pulverization as a dissipative process during seismic slip, Faulting, Friction, and Weakening: From Slow to Fast Motion, The Royal Society, UK, April 2526, 2016.
6. W.A. Griffith, T. Barber, C. Borjas, H.O. Ghaffari, INVITED, Experimental constraints on the energy budget of dynamic gouge formation: effects of rock strength, material heterogeneity, and initial flaw characteristics, EGU General Assembly, 2016.
7. H.O. Ghaffari and W.A. Griffith, W. Flynn, and R. P. Young, Measurement of Berry's Phase in Microscopic Cracking Excitations during Triaxial Rock Deformation, American Physical Society Meeting, March 14-18, 2017, Baltimore, MD.
8. C.D. Rowe, W.A. Griffith, C. Ross, B. Melosh, E. Young, Insights into earthquake rupture and recovery from paleoseismic faults, American Geophysical Union Annual Meeting, San Francisco, Dec. 12-16, 2016.
9. W.A. Griffith, H.O. Ghaffari, and T.J. Barber, Kinetic energy associated with dynamic fragmentation in brittle solids, American Geophysical Union Annual Meeting, San Francisco, Dec. 12-16, 2016.
10. H.O. Ghaffari and W.A. Griffith, Combined functional network and frequency-time analysis of acoustic emissions during cracking excitations, American Geophysical Union Annual Meeting, San Francisco, Dec. 1216, 2016.
11. R.C. Julien, H.O. Ghaffari, and W.A. Griffith, Microscopic observation of tremor-like excitations during dynamic loading of trapped liquids, American Geophysical Union Annual Meeting, San Francisco, Dec. 12-16, 2016.

d. Manuscripts

1. Ghaffari, H.O., W.A. Griffith, and T.J. Barber, Energy delocalization during rock fragmentation, in prep
2. Ghaffari, H.O., M. Pec, and W.A. Griffith, Supersonic localized excitations mediate microscopic dynamic failure, in prep

e. Books

-N/A

RPPR Final Report
as of 04-Sep-2018

Honors and Awards: 1. 2014 NSF Faculty Early Career Development (CAREER) Award – awarded to PI Griffith to study parallel problem of rock fragmentation during earthquake rupture
2. 2015 Outstanding Student Paper Award to Troy Barber for his presentation ", Controls on the formation of pulverized off-fault rocks: Laboratory investigations using Arkansas Novaculite" at the 2015 American Geophysical Union Fall meeting in San Francisco, CA
3. 2016 Outstanding Publication Award – Geological Society of America, Structural Geology & Tectonics Division - This award is given annually for a published work (paper, book, or map) of exceptional distinction that clearly advances the science of structural geology or tectonics. Award given for: Rowe, C.D. and W.A. Griffith, 2015, Do Faults Preserve a Record of Seismic Slip? A second opinion, Journal of Structural Geology,78, 1-26, doi: 10.1016/j. jsg.2015.06.006
4. 2016 Regents' Outstanding Teaching Award - Offered annually in recognition of faculty members at The University of Texas System's nine academic and six health institutions who have demonstrated extraordinary classroom performance and innovation in undergraduate instruction, the Regents' Outstanding Teaching Awards are the Board of Regents' highest honor.
5. 2016 Royal Society Invited Participant – Invited speaker at Theo Murphy international scientific discussion meeting on "Faulting, friction, and weakening: from fast to slow motion"

Protocol Activity Status:

Technology Transfer: Nothing to Report

PARTICIPANTS:

Participant Type: Graduate Student (research assistant)
Participant: Troy Barber
Person Months Worked: 1.00 **Funding Support:**
Project Contribution:
International Collaboration:
International Travel:
National Academy Member: N
Other Collaborators:

Participant Type: Postdoctoral (scholar, fellow or other postdoctoral position)
Participant: Hamed Ghaffari
Person Months Worked: 12.00 **Funding Support:**
Project Contribution:
International Collaboration:
International Travel:
National Academy Member: N
Other Collaborators:

Participant Type: PD/PI
Participant: William Ashley Griffith
Person Months Worked: 1.00 **Funding Support:**
Project Contribution:
International Collaboration:
International Travel:
National Academy Member: N
Other Collaborators:

DISSERTATIONS:

RPPR Final Report
as of 04-Sep-2018

Publication Type: Thesis or Dissertation
Institution: University of Texas at Arlington
Date Received: 09-Nov-2017 Completion Date: 12/1/16 8:22PM
Title: EXPERIMENTAL CONSTRAINTS ON THE MICROMECHANICS OF BRITTLE FRAGMENTATION DURING EARTHQUAKE RUPTURE
Authors: Barber, Troy
Acknowledged Federal Support: **Y**

This document contains two manuscripts nearing the final stages of presentation. These manuscripts are referenced within the main prose of our report. Detailed information and figures can be found in the manuscripts. The manuscripts contained in this document are listed below, and the types are hyperlinked to their location in the document.

Energy Delocalization during Dynamic Rock Fragmentation

H.O. Ghaffari [1], W.A.Griffith[2], and T.J.Barber[3]

[1]Department of Earth, Atmospheric and Planetary Sciences, Massachusetts Institute of Technology, Cambridge, Massachusetts, USA

[2] School of Earth Sciences, Ohio State University, Columbus, Ohio, USA.

[3] Department of Earth and Environmental Sciences, University of Texas at Arlington, Box 19049, Arlington, TX, USA

The formation of fragments due to avalanche-like growth of damage under impulsive forces is a process central to numerous studies ranging from shaped-charge jet break up and rock blasting to bolide impacts, and, more recently, earthquake rupture. In the latter case pulverized rocks found millimeters to tens of meters from the principal slip zone of large faults have been associated with fast, and even supersonic, rupture propagation. It has been postulated that earthquake source characteristics directly affect the degree of fragmentation and the study of fragment size distribution may shed light on the energy budget of individual earthquakes, as well as long term effects on fault zone properties. The actual fragmentation process, and the partitioning of dissipated energy at fast loading rates, however, is still enigmatic. We use modified Split Hopkinson Pressure Bar experiments, in which we can control stressing rate, amplitude, and duration, as a laboratory analog for the complex natural prototype source processes. In our experiments, we characterize the velocity distribution of ejected fragments from Westerly Granite specimens resulting in a range of fragmentation states, from weakly fragmented to pulverized. Analysis of the velocity distributions (and the related kinetic energy) reveals spatial domains that are free of ejected fragments; these so called “zero-kinetic energy modes” are related to the fragmentation state: increasing fragmentation corresponds to a reduction of zero-mode domains. Our results support recent theories in the solid-granular transition where the system under external impulsive-load transitions from an initial ground state (i.e., fully zero-mode) to another ground state (with null zero modes), implying the formulation of the solid-granulation transition can be described using phase-transition like theories. Furthermore, our results yield important insights into the process of fragmentation in earthquake process zones, including how dissipated energy is partitioned between surface and kinetic energy, and indicate that delocalization of energy is systematically coupled with source parameters.

Key Words

Fracture and flow; Fault zone rheology; Acoustic properties; Earthquake dynamics; Fractures, faults, and high strain deformation zones; Rheology and friction of fault zones

Introduction- The formation of fragments as the result of a sudden change of one or multiple control parameters is a common process in a vast range of fields from cosmology to material science (*Grady, 2010; Kibble, 1976; Curran et al., 1987*). In crystalline materials such as rocks, fragmentation is the transition from a solid to granular state as the result of initiation and coalescence of cracks. One of many geological manifestations of this transition is the formation of damage zone fractures around moving earthquake ruptures where the passage of an impulsive stress wave (or rupture front) induces a range of damage, from moderately fractured to completely pulverized (*Doan & Gary, 2009; Mitchell et al., 2011; Rempe et al., 2013*). In a geological context, "pulverized" rocks are characterized by intense fracturing, with insignificant grain rotation, such that the original fabric of the rock is preserved (*Dor et al., 2006; Doan & Gary, 2009)*. The pulverization state – in which the whole of the medium is finely and homogeneously fractured – is the regime in which energy localization is minimized, in contrast with the opposite expectation of maximum energy localization during propagation of a single crack. The dynamic transition from damage patterns characterized by a completely intact state to finite-sized fragments to the pulverized state is thus closely associated with the spatial energy distribution. It has been suggested that the fragmentation mechanism is a common process along crustal scale seismogenic faults with potential implications for source characteristics including the seismic energy budget (*Wilson et al., 2005; Rowe & Griffith, 2015*).

Dynamic uniaxial compression experiments on rock have shown that there exists a threshold strain rate at which the fragmentation transition from discrete failure at low strain rates to pulverization occurs (*Doan & Gary, 2009; Yuan et al., 2011*). While at lower strain rates, the energy (i.e., fracture energy) localized along a small number of cracks drives the system to the final state, increasing the

strain rate leads to the formation of small, finite domains in which the size of fragments varies inversely with the strain rate (or stress ramp) (*Grady & Kipp, 1987; Reches & Dewers, 2005; Grady, 2008*). In the former case, in which failure is dominated by a few localized cracks, the fracture energy dominates the dissipated energy, while the kinetic energy, which increases with the square of the strain rate, becomes increasingly important with faster stress ramps (*Grady & Kipp,1987; Zhang & Zhao, 2014; Bazant & Caner, 2014*). The interplay between these two energy terms is likely key to determining the fragmentation-pulverization transition, and the sum of these energy terms at fragmentation has been posited to control the ultimate fragment size (*Grady*, 1982; *Grady & Kipp, 1987*). Here, we explore the behavior of fragments emitted during fragmentation at a range of strain rates to characterize the evolution of the kinetic energy term and its relationship to particle size reduction. By analyzing the velocity and size of fragments, we identify a transition mode, described by a scalar damage parameter. The damage parameter is characterized by the prevalence of zero-kinetic energy modes, defined – as discussed below – by the spatial distribution of kinetic energy during fragmentation. The transition from a fully zero kinetic energy state to a finite number of non-zero modes and further to the null state can be described by a system driven between two ordered states by an external driving control parameter (i.e., stress ramp) (*del Campo & Zurek, 2014; Laguna & Zurek, 1997; Hakim & Karma, 2009*).

Our analysis is based on new experiments in which the impact pressure of flying fragments is imprinted on calibrated pressure-sensitive thin films surrounding the cylindrical rock samples. From the resulting spatial pressure distributions formed by fragments impacting the thin films, we infer the full spatial (normal) velocity components of ejected fragments, preserving a snapshot of the spatial distribution of kinetic energy in each experiment. Furthermore, we show that the degree of energy localization is amplified with decreasing strain rate, and that a damage parameter – closely associated

with the kinetic energy – characterizes the recorded patterns. Our results are consistent with recent theories of solid-granulation transitions, where a system under external impulsive load transits from an initial ground state (i.e., fully zero-mode) to another ground state (with null zero modes), implying the formulation of the solid-granular transition can be described using phase-transition like theories (*Lyakhovsky et al., 2016; Lyakhovsky & Ben-Zion, 2014; Truskinovsky, 1996*).

Experimental Procedure - The samples used consist of dry Westerly Granite, cored from the same block. We measured the P-wave velocities in different direction of the large 12" x 6" x 6" block and along radial directions of prepared cylindrical samples prior to tests. The average velocity in all measured directions is isotropicwith acoustic velocity of 4340±100 m/s. To assess the extent of intragranular damage in post-mortem fragments, we measured the P-wave velocity in fragments after experiments using handmade pinducers (i.e., needle-like piezoelectric transducers) with a tip size of 0.5 mm. We measured each fragment two times in the shortest and longest length scales of each fragment and took the average.

To understand the effect of impulsive stresses on the damage state, we conducted experiments aimed at understanding the effect of high strain rates ($\sim 10^1$-10^3 s^{-1}) on the fragmentation to pulverization transition of intact, dry Westerly Granite. The experiments were carried out using a Split Hopkinson Pressure Bar (SHPB) apparatus where an impulsive compressive stress pulse is generated by a cylindrical steel projectile (the striker bar). The striker bar impacts an incident bar of identical material and diameter (Fig.1a), and, using standard pulse design techniques (*Xia et al., 2008; Frew et al., 2002*), we control three main parameters of the source: peak magnitude, total duration, and ramp (strain) rate (Fig.1c). The source signal is transferred through the incident bar and interacts with the dry, cylindrical Westerly Granite rock sample. We consider the deformation history of the specimen

as representative of a volume of material adjacent to a passing fault rupture tip during earthquake propagation.

The cylindrical rock specimens are machined to ensure that ends are mutually parallel and orthogonal to the axial direction, prior to being placed between the incident and transmitted bars surrounded by a steel capture ring (Fig.1b-*Huang et al., 2014*). The sample is a few millimeters longer than the capture ring, such that the ring is not engaged by the incident bar until after the sample has failed completely. The radial distance of the sample from the interior surface of the ring is about ~2.75mm, allowing reasonable expansion up to ~25% strain and finite flying distance of the ejected particles due to fragmentation of the sample (Fig.1b). This also means that fragmentation is likely near its final state by the time rock particles reach the ring. Deformation in the incident and transmitted bars is monitored by strain gauges and the stress, strain, and strain rate histories experienced by the specimen during each experiment are calculated using standard methods (*Chen and Song, 2014*). We also used a third strain gauge on the capture ring to mark the time at which the ring is engaged to confirm that it does not interfere with deformation until after the sample has failed and lost load bearing capability.

To record the patterns of damage and estimate the velocity of ejected fragments, we line the interior surface of the steel control ring with thin pressure measurement film (Fujifilm Prescale Medium) that we have carefully calibrated for impulsive loads and short contact times (see Supplementary Material). The film is polyethylene based and has a thickness of approximately 110 μm. The film has embedded microcapsules (5μm resolution) that, when compressed, release ink with color intensity proportional to the applied pressure (*Selvadurai & Glaser, 2015*). Calibrated for contact times similar to those in our experiments, the film records a range of dynamic stress amplitudes from ~10MPa to 150MPa (see Supplementary Material). We assume that the film (capsules + Polyethylene

layers) has an elastic response for up to 13% dynamic strain (*Xu et al., 2016*) yielding a 15-20 μm elastic deformation regime. Reducing the allowed elastic penetration depth results in a narrower particle size distribution as discussed below. After each test we scanned the pressure films with resolution of 1024×1024 dpi. Depending on the color of each cell a dynamic stress is assigned based on our empirical dynamic calibration.

We use an elastic *Hertzian* contact approach to convert the pressure distributions recorded on the thin films to particle size and velocity distributions as they impacted the film. In this approach, we assume that the velocity vector is perpendicular to the thin film. The pressure films per each test estimate a local pressure, *p* (for a given pixel on the film). The maximum penetration depth on the film is given by (*Johnson, 1987*):

$$\delta_{\max} = \left(\frac{15 m V_{app}^{2}}{16 < \xi >^{1/2} E^{*}}\right)^{2/5}, \qquad (1)$$

where *m* is the mean mass of each fragment , $V_{app.}$ is the colliding velocity and $\frac{1}{E^{*}} = \frac{1-\upsilon_{particle}^{2}}{E_{dynamic}} + \frac{1-\upsilon_{film}^{2}}{E_{film}}$ with $E_{dynamic}$ as the dynamic Young modulus for the dynamically loaded fragments and E_{film} is the Young's modulus of the film. We can estimate the maximum force based on recorded pressures:

$$F_{\max}^{i} = p_i S_{indent} = K \delta_{\max}^{3/2} \qquad (2)$$

with $K = \frac{4}{3} < \xi >^{1/2} E^{*}$ and S_{indent} is a function of $\delta_{\max}$ (see Supplementary Material for the full expression). We can then derive:

$$p(r,\theta) \approx \frac{4K\delta(r,\theta)^{\frac{3}{2}}}{\left(\frac{2\delta(r,\theta)}{< \xi >} + \frac{\pi}{2} - 1\right) < \xi >^{2}}, \qquad (3)$$

Therefore, assuming a bound for penetration depth $\delta \in [\delta_{\min}, \delta_{\max}]$ and having calibrated the imprinted pressure on each pixel of the scanned film (Fig. S4), we can estimate a range of maximum colliding

velocities and fragment sizes for a given element on the pressure film (Fig. S2). We consider a range of 500 possible particle sizes, employing higher frequency binning for the finest particles. For a given pressure value, we calculated an upper and lower ranges of velocity with given penetration bound. This procedure yields an average value of collision velocity ($(V^i_{app})_{p=p^*} = \frac{V^i_{\min} + V^i_{\max}}{2}$) for each class which is associated with a fragment size and the known pressure (see Fig.S2).

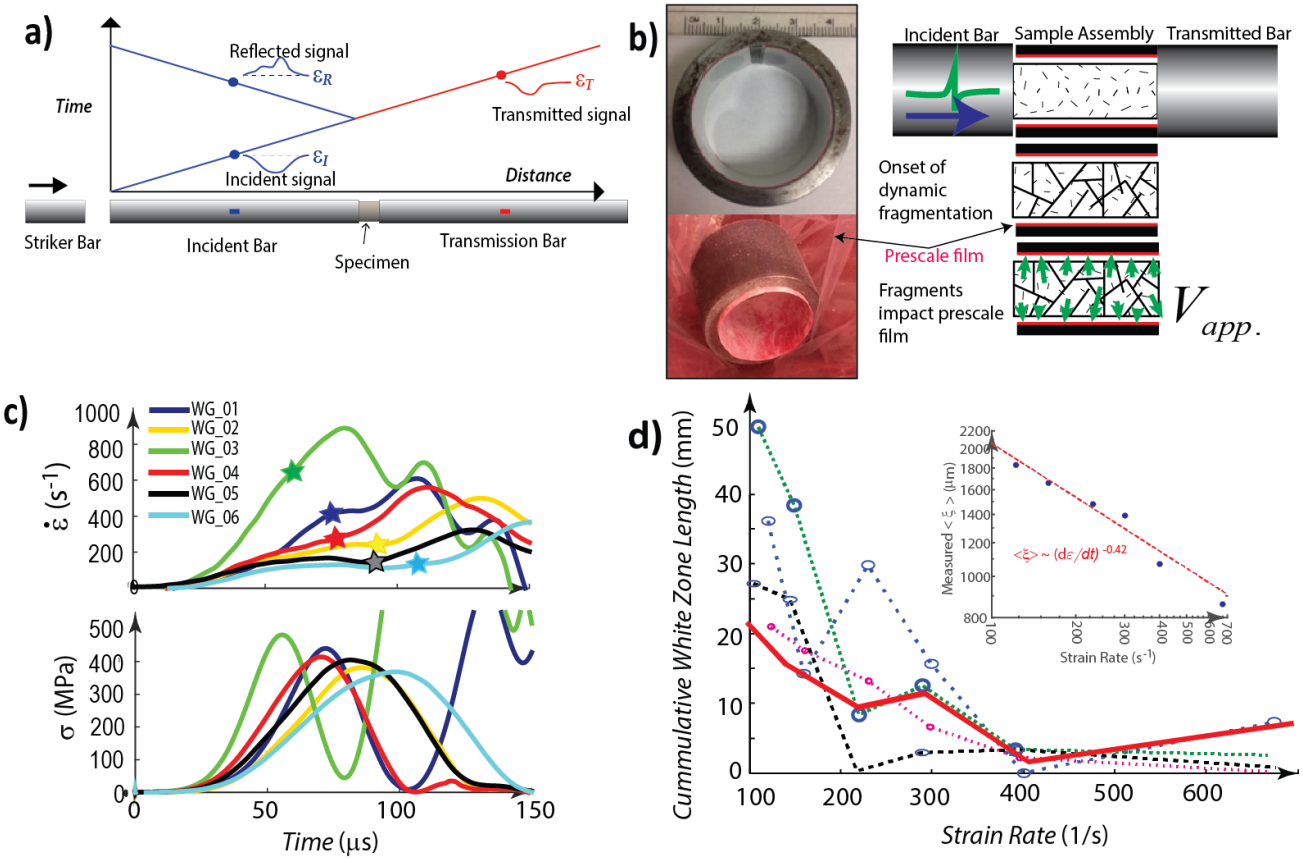

Figure 1| Experimental procedure. a) The rock specimen and capture ring is placed in Split Hopkinson Pressure bar apparatus. The amplitude and the duration of the incident signal is tuned by small copper pulse shaper mounted at the interface of striker bar and incident bar. The striker bar acts like a *pump* and the reflected and transmitted dynamic gauges probe the signals. **b)** The interior of a capture ring is lined with a thin film (Fujifilm Prescale Medium pressure measurement film). Upon brittle failure and fragmentation, the flying fragments hit the thin film and imprint a color change proportional to maximum induced normal pressure (See Figure 2). **c)** Recorded strain rates and stresses for different ramps on 6 Westerly granite samples. The star denotes the critical strain rate as the onset of fragmentation/pulverization. In all our cases studies, we satisfy the dynamic force equilibrium condition to extract stress, strain, and strain rate time series. **d)** White (~zero stress) and red patterns are recorded on the pressure films (see Fig.2a). Cumulative size of white zones versus strain rates represents the evolution of damage level of the rock samples (the thick red line). The dotted profiles are randomly selected circumferential profiles (rings) along the sample. The thick red line is averaged over all circumferential profiles. Note that for slow ramp rates, the localized fracture energy is dominant and the damage patterns on the pre-scale films are white and "silent". Inset: faster strain rates result in smaller fragments, well described by a power-law with exponent b≈0.42.

Results-

To proceed, we deform specimens at peak strain rates from 50 1/s to 900 1/s (Fig.1b) and monitor the resulting patterns encoded in the pressure film for each experiment. The patterns recorded on each pressure film reflect a "frozen" snapshot of the fragmentation process for each experiment (Fig.1a). Interestingly, at lower strain rates (i.e., pulses with longer rise times) a significant portion of the unfolded surface of the thin films is covered by networks of white zones surrounding islands of color. By increasing the intensity (strain rate and stress amplitude) of the source, the thickness and distribution of the white web-like patterns change and much of the film becomes colored. We interpret these white patterns to be related to physical fragmentation boundaries. To quantify these patterns, we first select random profiles perpendicular to the loading direction (i.e., circumferential profiles from 0-2π; Fig.2a) and calculate the cumulative size of white zones in that profile for different strain rates (dotted lines in Fig.1d). Averaging over all profiles for each experiment, we observe a general trend of reducing area occupied by white zones with increasing ramp rate, consistent with qualitative observations (Fig.2). Later we will show that these patterns are quantitatively related to the net damage imparted to the samples.

We idealize the ejected particles as spherical fragments, with average characteristic radius $<\xi>$, that collide elastically (*i.e.*, velocity-dependent Hertzian contact [*Johnson, 1987*]) with the thin film along a velocity vector normal to the film. Based on a maximum allowed penetration depth of 20μm and our empirical color calibration curve (see Methods and SI), we can assign a velocity and a particle size for each pixel of the scanned film. As a result of this heuristic algorithm, particles with smaller size and greater terminal (normal) velocity imprint higher stress (and deeper penetration)

yielding greater color change. It is noteworthy that fragments with large characteristic size are assigned almost zero velocity (zero-kinetic energy mode) and finer fragments tend to be associated with higher impact velocity. The maximum calculated velocity was ~50m/s which occurs for particles with <400 μm diameter for experiment WG-03 (strain rate 675 1/s). The upper limit of the particle size from this method is ~850-990 μm. Employing pressure films sensitive to smaller pressure would increase this range, but these films would be easily saturated under the present testing conditions. While we used several assumptions in the estimation of normal components of the velocity field, our results are comparable with similar dynamic tests (at the same order of ramp rate) and direct – but more coarse - measurement of the radial velocity field (*Frew et al., 2002; Huang et al., 2014*).

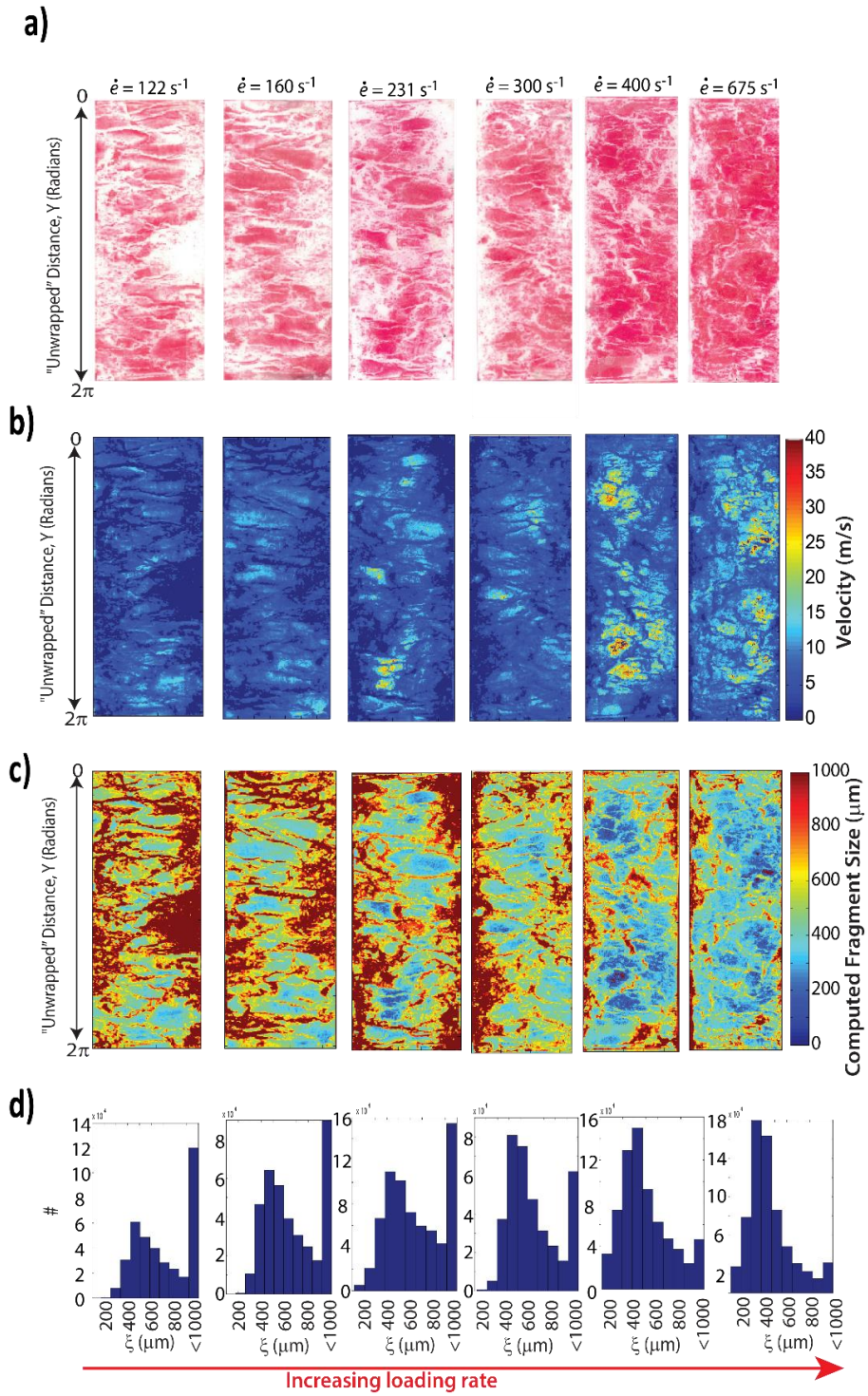

Figure 2| Fragmentations patterns encoded on pre-scaled films. a) Raw recorded patterns of thin pressure film surrounding the sample for different strain rates. The y-direction has been unfolded in along the circumference and the x-axis is the axial direction along the sample. **b)** Inferred spatial normal components of velocity based on Hertzian contact mechanics. **c)** Estimated fragment size for the colliding particles based on a maximum penetration depth of 20μm and for spherical particles. Based on the results of panels (b) and (c) we approximate the kinetic energy component and the distribution of particle sizes in the range of the pressure films. (d)_Estimated fragment size distribution using pressure distribution from prescale films.

Next, we compare the estimated distribution of fragments with the post-mortem analysis of particle size distribution from our experiments (Fig3.a & b). Grady (1982) suggested a connection between average particle size and strain rate during fragmentation by considering an expanding sphere and identifying the total particle surface area at which the sum of the kinetic and surface areas are minimized. The result led to a relationship between average particle size D and strain rate $\dot{\varepsilon}$ in the form $D(\dot{\varepsilon}) \propto \dot{\varepsilon}^b$, with exponent $b = 2/3$. In what follows we analyze the particle size distribution to test this prediction.

Analysis of the real particle size distribution shows that with increasing strain rate, mean fragment size is reduced by ~ 47% (see supplementary information Fig.S.5). Since the range of fragment size estimated indirectly from the pressure film has an upper bound of ~0.9 mm, smaller than the largest fragments directly measured, and because (as will be shown below) the bulk of kinetic energy is invested in particles less than that size, we use a weighted particle size distribution for both the measured and estimated fragment size distributions where we modify the particle sizes based on residual mass of the particles.

The measured and estimated particle size distributions are modified based on the following procedure. We modify the particle size intervals by assigning a "weight" w_j, given by $w_j = \frac{\sum_{i=1}^{m \le n} m_i^{\le \xi_{990\,\mu m}}}{\sum_{i=1}^{n} m_i}$ where $m_i^{\le \xi_{990\,\mu m}}$ is the mass of fragments in a given bin $[\xi_i, \xi_{i+1}] \le 990\mu m$; n and m are the total number of bins and the number of bins with less than $\xi = 990\mu m$, respectively. Note that m_i for measured particles are measured masses, whereas for estimated distributions m_i are calculated based on total fragment volume and density of Westerly Granite. Then for bins with $\xi \ge 990\mu m$, we have $w_j = 0$ and for fragments smaller than 990 μm, the modified fragment size is given by $D_w^j = w_j \xi_j$.

This procedure reduces the mean size of measured particles from ~0.64mm to ~ 0.48mm over the range of strain rates examined (i.e., ~25% reduction). The relative change in the mean estimated particle size distribution is from 0.5mm to 0.35 over the same strain rate range (~20% reduction) which is in good agreement with the real change in mean fragment size. Comparing the power law exponents (b-value in $D(\dot{\varepsilon}) \propto \dot{\varepsilon}^{b}$) between the calculated (0.18) and the weighted measured (0.12) fragments shows good agreement; the exponent is larger (0.42) when considering all measured particles including the coarse size fraction (Fig.S6). The smaller exponents from our calculated and weighted measured fragments emphasize the fraction of particle sizes that contribute significantly to the post-fragmentation kinetic energy.

When compared with the total dissipated energy, the estimated kinetic energy (based on the estimated average velocity and summation of the ejected mass) indicates on first inspection that the kinetic energy based on isotropic source is a small fraction (maximum ~7 %-Table 1) of the total dissipated energy, and generally smaller than the energy used to create new surface area (*Barber and Griffith, 2017*). For example, when fragmentation occurs at a strain rate of 675 1/s, the dissipated energy in the system is about ~410 J. Here, the dissipated energy in the system includes: (1) internal friction of bars; (2) frictional effects in boundaries between bars and rock sample; (3) the frictional effects between the formed particles, (4) cumulative fracture energy (the energy required to overcome binding and cohesive forces between molecules and atoms to create new surface area); (5) kinetic energy of the bulk body; and (6) other energies dissipated in emitting higher energy waves (such as ultrasound waves or electrons). During elastic experiments (i.e., experiments in which no apparent inelastic deformation occurs in the specimen) we have found energy losses due to (1) and (2) to be very small. Conversely, surface energy (5) in similar experiments can be ~5%, or perhaps larger considering potential measurement error, of dissipated energy (*Barber and Griffith, 2017*). We expect

that the initial kinetic energy of fragmented particles may have been substantially larger than the kinetic energy measured using the pressure film, but that subsequent energy dissipation due to frictional contact between particles during the incipient stages of fragmentation and particle acceleration is a substantial energy sink during the fragmentation process, as has been hypothesized previously *(Bažant and Caner, 2014; Ben Zion and Sammis, 2013)*.

Table 1| Summary of Energy Terms

Sample #	$W_{incident}$(J)	$W_{reflected}$(J)	$W_{transferred}$ (J)	$W_{Dissapted}$ (J)	$W_{kinetic\ energy}$ (J)	dε/dt (max)
1	430	180	95	160	10.7	400
2	310	145	35	130	4.82	230
3	1015	400	205	410	12.5	675
4	280	170	30	80	4.8	300
5	165	60	40	65	3.2	160
6	175	80	40	55	2.1	120

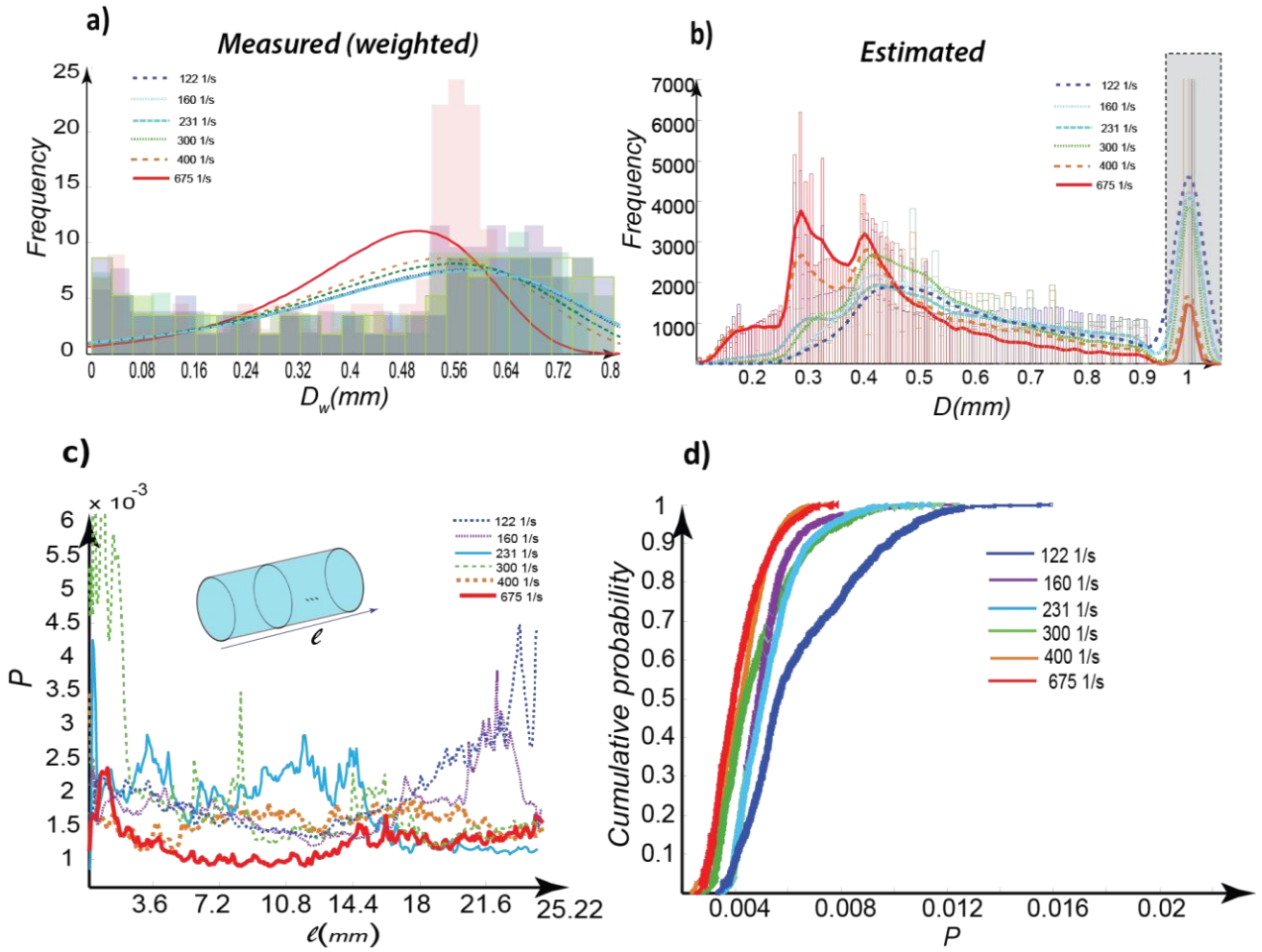

Figure 3| Fragment size distribution. (a) Measured distribution of fragments for successively increasing ramp rate. We considered particles below 900μs and modified the values based on a reduced weight factor. The lines are fitted (extreme value distribution) to the particle size distributions **(b)** Estimated fragment size distribution using pressure distribution from prescale films. Increasing strain rate shifts the mean of fragment size to lower values. A transition from single peak to double peak is observed for 400 and 675 *1/s* strain rates in estimated distribution. Increasing number of fragments (smaller fragments) agrees with lowering the zero-modes encoded in the peak of distribution ($D \geq 1$(mm)). **(c,d) Localization of colliding velocity vectors:** a scalar measure (*P*) characterizes the localization degree of vectors. A higher value of *P* corresponds with a higher degree of localization. Here we show the degree of localization per each profile (ring) along the sample length. Increasing the ramp rate lowers the degree of energy localization, such that P becomes uniform and approaches zero (red curve). In (**d**) we show the cumulative probability distribution of P versus different strain rates. The probability of finding less-localized vectors increases with increasing ramp rate, which coincides with production of finer fragments and increasing degree of pulverization. An ideal fully pulverized state $P \rightarrow 0$.

Now we turn our attention to analysis of normal components of the velocity field (Fig.2b). We define a scalar parameter for each given circumferential profile that characterizes the localization degree of an array - also called the inverse participation index, ***P*** - defined by [*Kuramoto,1984;*

Ghaffari&Young ,2012]: $P(v) = \frac{\sum_i (v_i)^4}{(\sum_i (v_i)^2)^2}$. For the maximum value of ***P*** the profile has only one non-zero component, corresponding to a more localized vector. For each circumferential profile, ***P*** is calculated (Fig.3c), and indicates that increasing the strain rate corresponds to a reduction in kinetic energy localization as expected. This feature is particularly well illustrated by the cumulative probability distribution of ***P*** values: the probability of finding less localized vectors increases by increasing the strain rate which coincides with producing finer fragments and, therefore, increasing degree of fragmentation (Fig.3d). We can infer that an ideal, fully pulverized state corresponds to $P \to 0$. We find a significant rate dependence on shifting the localization degree, which coincides with decreasing fragment size (Fig.3b) as well as increasing the material yield strength (Fig.1c).

Next, we calculate kinetic energy $E_{kinetic} = \frac{1}{2}\sum_{i=1}^{N} m_i (\frac{du_i}{dt})^2$ and represent the angular distribution of E_{kinetic} in separate upper ($0 < \theta < \pi$) and lower ($-\pi \le \theta \le 0$) circumferential spaces (Fig.4a & b). The resulting energy-space spectrum represents the velocity field anisotropy for the upper and lower hemispheres where for slower ramps the anisotropy is more pronounced (Fig.S8). For instance, at $\dot{\varepsilon} = 122 s^{-1}$ and considering a single circumferential profile, the average slope of the spectrum $\frac{\partial E_k}{\partial \theta}$ (i.e., dotted lines in Fig.4a) in the lower hemisphere is higher than the upper hemisphere. At higher ramp rates (Fig.4b) anisotropy is less pronounced, coinciding with more delocalized energy as described earlier. Moreover, the zero-energy modes can be visualized in the angular distribution of velocity vectors (insets of Fig.4a, b) in which the zero-kinetic energy components lie on the reference circle. In very high strain rate experiments, we could find profiles devoid of zero-components (Fig.4b), indicating all measured elements on the 1D-cicumerfential profile carry significant kinetic energy

leading to complete disintegration of the initial profile. This is a pulverized state in comparison with the state where the profile includes a finite number of zero-modes. Therefore, zero-energy modes of the samples mapped on the pressure measurement film can be used to characterize the transition from a fragmented state to an ideal pulverized regime in terms of energy localization-delocalization.

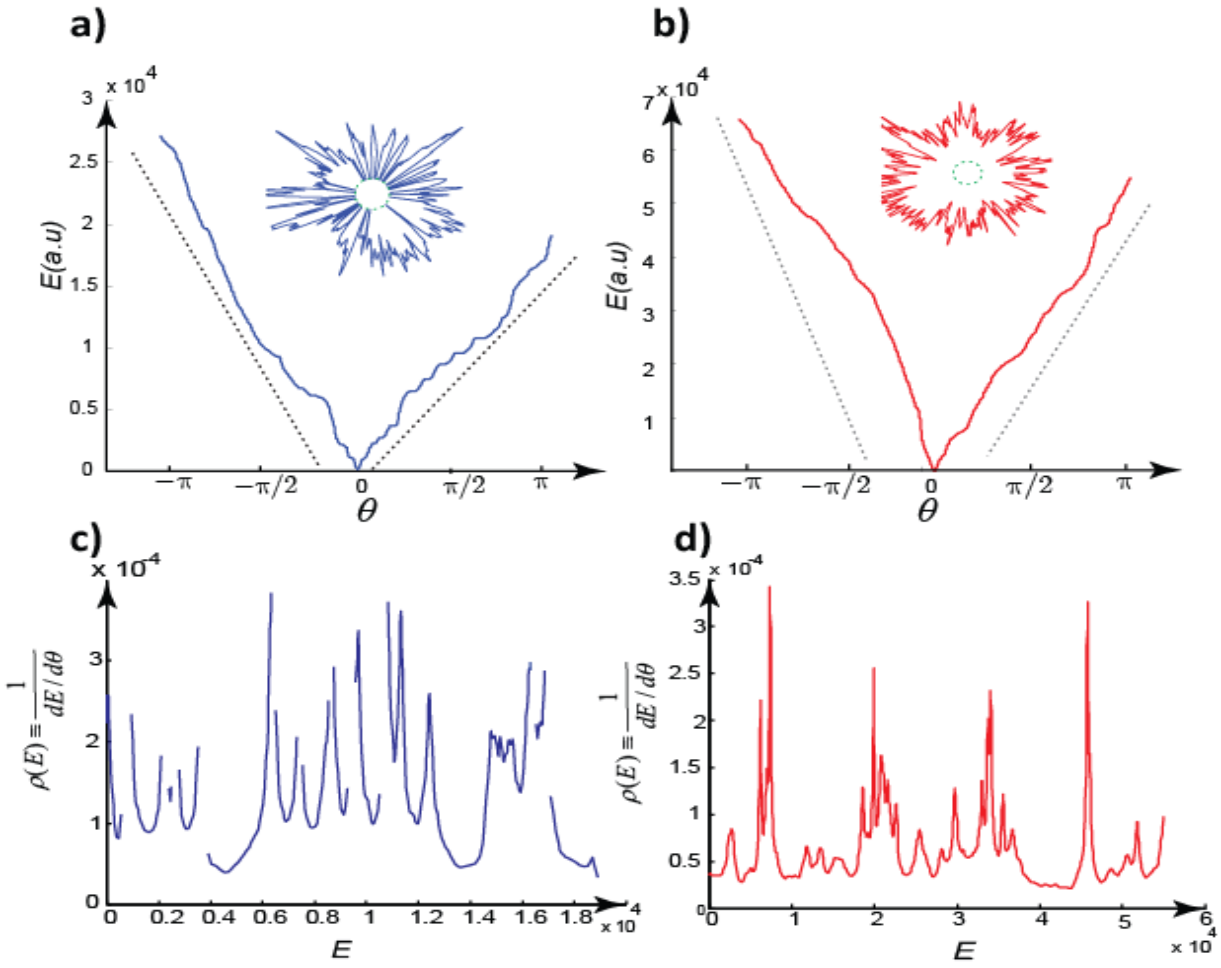

Figure 4| Spectrum of kinetic energy for fragmented and pulverized states. (a) The energy spectrum of a given circumferential profile (from the experiment with $\dot{\varepsilon} = 122s^{-1}$ in arbitrary units (a.u)) for upper ($0 < \theta < \pi$) and lower ($-\pi \le \theta \le 0$) hemispheres. Inset: calculated normal component of the colliding velocities. The green circle is the zero-kinetic energy state. **(b)** Same as (a) for $\dot{\varepsilon} = 675s^{-1}$. The profile in the inset has null-zero energy modes and is in opposite state of full zero-energy mode state (i.e., green dotted ring). The dotted black lines indicate average slope of the spectrum, significantly sharper than the case (a). **(c, d)** The density of states versus energy shows finite number of singularities in fragmented state while these states are eliminated in an ideal pulverized state (i.e., fully ordered state). Upper portion of the profiles are shown in the insets of panel (a) and (b).

We map the angular direction along a given circumferential velocity profile on to a vector $\mathbf{k}$ with fixed magnitude and direction Θ. Therefore, a system with N elements is characterized by $\mathbf{k}$ vectors and the energy E_k is defined in $\mathbf{k}$-space ($E_k(\mathbf{k})$). For a 1D profile, the length of each vector point is $\Delta\mathbf{k} = \frac{2\pi}{l}$ (l is the length of the profile) and we can define $dN = \frac{l}{\pi}\int_{\theta}^{\theta+d\theta} d\mathbf{k}$ as the number of elements from Θ to $\Theta+d\Theta$. For fully uniform systems (intact or uniformly pulverized) all elements occupy a "state" in $\mathbf{k}$-space. Note that by mapping the profiles to $\mathbf{k}$-space, we indirectly consider a virtual quasi-1d lattice with certain number of sites and therefore we could map the patterns on to a $\mathbf{k}$-E space and obtain dispersive-like curves (Fig.4a,b). Next, we show that zero-energy modes form singularities in the energy spectrum. To characterize the energy distribution in $\mathbf{k}$-space, we use the concept of density of states as [*Harrison ,2012; Kittel ,1966*]: $\rho(E_k) = \frac{l}{2\pi\left|\frac{dE_k}{d\theta}\right|}$ (or $\rho(E_k) = \frac{1}{l}\left|\frac{dN}{dE_k}\right|$). For a fully pulverized state, the $E-\rho(E$) space is continuous with fluctuations showing a denser energy state in that section of space. Adding zero-energy modes to the profile results in a finite number of singularities with a sharp state at the point of the zero-mode (Fig.4c). We interpret this transition from a single state (pulverized or intact) to a mixed state as the fragmentation-pulverization transition. The mixed state includes a finite number of singularities equal to the number of zero-modes, and therefore from this perspective we can propose the following scenario: our system transits between two ideal ordered states (intact to fully pulverized), and adding zero-modes increases the disorder in this system; therefore the mixed state is the transition from the ordered to more disordered state. This implies that the observed singularities in density profiles of the kinetic energy spectrum are "defects" which induce disorder to either of the pure states. We note that, based on this observation, the transition between two pure states occurs smoothly as a continuous transition. Having a state (or phase) parameter and

an external control parameter, as well as continuous transition between two ordered phases, the problem can be formulated in terms of a second-order phase transition, well described by *Landau-Ginzburg*'s equation (or phase-field models- *Hakim&Karma ,2009*]; Fig.S9). Recently, there have been several attempts to describe the solid-granular transition in the context of phase transitions [*Lyakhovsky, et al., 2016; Lyakhovsky, 2014*], and our observations validate this approach.

While in the above analyses, we assumed each fragment is an ideal elastic object, our measurements using ultrasound probes on post-mortem fragments show dramatic reduction of P-wave velocity, indicating substantial internal damage in fragments (Fig.5). The post-ultrasound measurement of P-wave velocity in fragments with characteristic size >0.5 mm showed that in some fragments the velocity can drop up to 1200 m/s which indicates the growth of micro-cracks within a macroscopically cohesive fragment. This shows that the internal damage state of each individual fragment will not necessarily be captured with thin films and the recorded patterns are associated with kinetic energy based damage in terms of disintegrated fragments where each fragment is in an apparent intact state. Another implication of these measurements is that estimating surface energy via measurement of exposed fragment surface area (by, for example, BET surface analysis, e.g., *Barber and Griffith, 2017*) may not capture the fraction of dissipated energy consumed in generation of microcracks within the fragments.

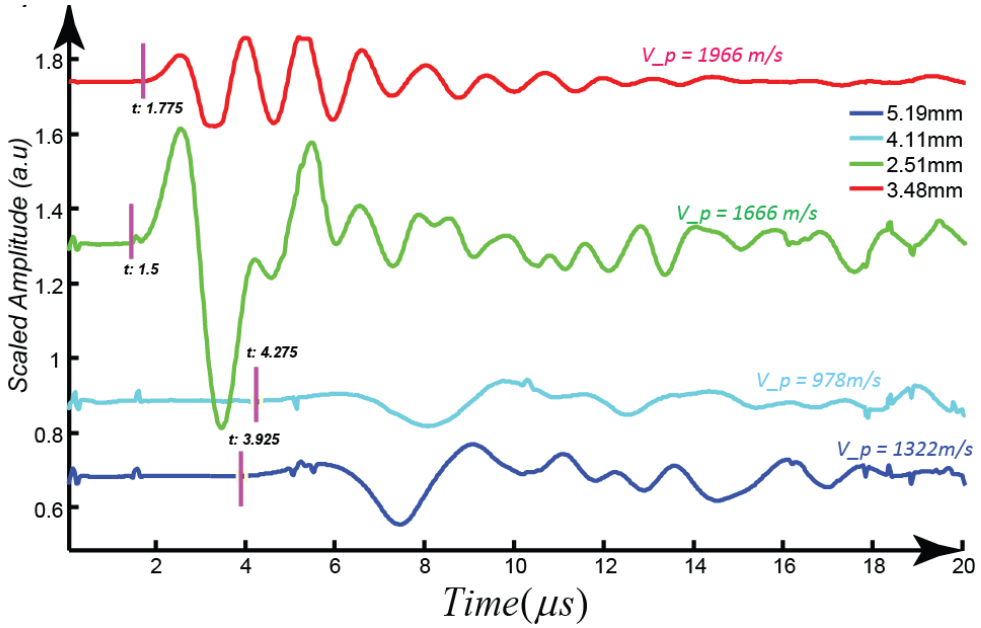

Figure 5| Measurement of sound velocity in (a) fragmented pieces with pico-PZT transducers. Before measurement, we calibrate the sensors with connecting them face-to-face and read the delay time (~0.3μs). The measurement of sound velocity of intact Westerly granite (WG) with similar method result 4.3 km/s. we show examples of Measurement of sound velocity in fragments from WG-2 case study with needle-like piezo transducers. The *p-arrival* times are marked with vertical purple lines. These result show that apparent cohesive fragment inherit substantial damages after impulsive loads.

Discussion- We have described a series of dynamic fragmentation experiments in which the full velocity field of flying fragments was inferred at the onset of fragmentation. By analyzing spatial velocity patterns, we established that the interplay between localized and delocalized components of energy is not trivial and dictates the mean particles size. This interplay is well-described by the damage parameter $D(\dot{\varepsilon})$.

Our results not only mark the importance of understanding the mechanism of grain size reduction (akin to the formation of pulverized damage zone rocks and gouge materials *[Dor et al.,2006 ;Olgaaard,1983*]), but they also suggest that careful analysis of *frozen* patterns of fragmentation sheds further light on the source parameters as well as energy flow in the vicinity of moving fault ruptures. Consider the implication that neither kinetic nor fracture surface energy constitute a substantial dissipative energy sink in the present tests. Nielsen et al. (2016) observed that measures of breakdown

work estimated from high-velocity friction experiments showed a remarkable similarity to seismological estimates of fracture energy dissipated during natural earthquakes, but that the similarity only held for total slip displacements less than ~ 10cm, beyond which the seismological estimates dramatically surpassed those observed in the laboratory. The authors suggested as one possible source of the discrepancy, inelastic yielding and associated fragmentation in the wall rocks that occurs during *large* (slip $\geq$ 10m) earthquakes, for which this dissipative term becomes an increasingly significant part of the seismic energy budget and is inherently absent in lab-scale frictional slip experiments; yet estimates derived from fracture surface area measurements in the damage zones of crustal-scale faults indicate that surface energy constitutes an insignificant dissipative sink. If intergranular friction-generation occupies a substantial portion of the fragmentation energy budget, as suggested in our study, then substantial damage in the bulk would augment frictional heat generation along faults.

In the geological literature the term "pulverized" is reserved for rock textures in which grain size is reduced by nonsystematic brittle fractures such that the total strain is small and free from distortion [*Doan &Gary ,2009 ;Grady&Kipp,1987*]. Our observation challenges the common perceptions that such "pulverized rocks" are pure-states and ignores the potential micro-complexity of the fracture patterns. For example, anisotropy preserved in fracture patterns and elastic wave velocity in fault damage zone rocks, and the source of this anisotropy remains enigmatic [*Zhang&Zhao,2014]*; however, a potential explanation may be that the so called "pulverized" rocks may reflect a mixed state, a superposition of the pure intact and pure pulverized states as demonstrated in Figure 4. In our experiments, the faster global stress pulse yields finer average particle size and a uniform, delocalized energy state; a pure delocalization of energy leading to complete disintegration of the fragmenting material might be assumed as the perfect (absolute) pulverized state which results in particles as small as the atomic lattice distance (0.2-0.8 nm). This may imply that some details about the source (stress,

strain rate) may be encoded in anisotropic fragmentation of rocks in the field. Furthermore, the term "pulverized" may need to be reallocated for only special cases of fragmented rocks, as the current definition may lead to the neglect of important information.

The effect of microstructures, including grain size, grain shape and porosity, and initial intra-grain defects, effectively change the rate of evolution of the damage parameter and will be imprinted in power-law exponent of $D-\dot{\varepsilon}$ space as well as the developed patterns in the spatial energy distribution maps. The energy patterns in our studies are end-products of experiments and cannot unravel the local mechanisms controlling microcrack nucleation, propagation and arrest that form the observed string-like networks; however, establishing a direct connection to a continuous state (phase) transition and employing a dynamic phase field equation with a control parameter yields local evolution of the order parameter and final mean domain size (i.e., damage parameter) [*kibble ,1976; Laguna&Zurek ,1997*].

Our results also have interesting implications for energy-based fragmentation models (e.g., Grady model), particularly as such models have been utilized to try to interpret transient source parameters by examining fragmentation textures along exhumed faults and bolide impact structures [*Key&Schultz,2011*]. Such energy-based models, which predict relationships between strain rate and fragment size by considering the transformation of local kinetic energy in isotropically expanding bodies to fracture energy based on, for example, an assumption of energy minimization, typically underestimate fragment size at slow strain rates while overestimating fragment size at higher strain rates [*Zhou et la.,2005*]. Our results show some consistencies with such fragmentation models, namely that the local kinetic energy of flying fragments is strongly related to final fragment size; however, the fact that our *b* exponent of 0.42 is smaller than the $b = 2/3$ exponent of Grady [*Grady ,2008*] suggests that the complexities of compressive failure in complex polycrystalline materials are not well-captured

in such models. Given the small percentage of total dissipated energy (<50%) captured by analysis of surface area (*Barber and Griffith, 2017*) and *final* kinetic energy in this study, that complexity is likely a very important part of the compressive fragmentation process. Furthermore, the *b* exponents in our modified fragment size analysis suggest that kinetic energy is dominated in the later stages of fragmentation by only a subset of the fragmented particles (i.e., the smaller sizes).

In our estimation of the radial velocity field, we assumed that the oblique components of the velocity vectors are negligible (i.e., local shear component of each separated fragment is trivial). However, during any quasi-1D dynamic loading tests (compressive or tensile), not all local source mechanisms are necessarily pure compressive or dilatational and mixed sources occur due to interactions of grains. Estimation of shear components of the ejected fragments would shed further lights on frictional forces leading to a non-negligible heat energy term [*Ben-Zion &Sammis, 2013*].

Further study is needed to distinguish response of rock materials to pure tensile or shear stress pulses where the state of the material is dynamically altered to a highly fragmented state. We propose that the captured spatial energy distribution due to ejected or high energy particles in tensile or shear stress dynamic pulsing will result in quantitatively different patterns and will also affect the microstructure of the fragments. For dynamic shear (e.g., torsional pulses) tests, due to importance of oblique components of the velocity field, the presented methods must be modified to take into account these shear-based sources.

Supplementary Information

Supplementary information accompanies this paper.

Acknowledgements

Research was sponsored by the Army Research Laboratory and was accomplished under Grant Number W911NF-14-1-0876. The views and conclusions contained in this document are those of the authors and should not be interpreted as representing the official policies, either expressed or implied, of the Army Research Laboratory or the U.S. Government. The U.S. Government is authorized to reproduce and distribute reprints for Government purposes notwithstanding any copyright notation herein.

Author Contributions

All authors contributed to analysis of the results and contributed the writing of the manuscript. H.O.G and W.A.G. co-wrote the manuscript. T.J.B, H.O.G. and WAG designed the main tests and performed the experiments. W.A.G supervised the research and helped to analyze the results.

Competing financial interests

The authors declare no competing financial interests.

References

[1] Barber, Troy, and W. Ashley Griffith. "Experimental constraints on dynamic fragmentation as a dissipative process during seismic slip." Phil. Trans. R. Soc. A 375, no. 2103 (2017): 20160002.

[2] Bažant, Z.P. and Caner, F.C., 2014. Impact comminution of solids due to local kinetic energy of high shear strain rate: I. Continuum theory and turbulence analogy. Journal of the Mechanics and Physics of Solids, 64, pp.223-235.

[3] Ben-Zion, Y. and Sammis, C.G., 2013. Shear heating during distributed fracturing and pulverization of rocks. *Geology*, *41*(2), pp.139-142.

[4] Curran, D.R., Seaman, L. and Shockey, D.A., 1987. Dynamic failure of solids. Physics reports, 147(5-6), pp.253-388.

[5] del Campo, A. & Zurek, W. H. Universality of phase transition dynamics: Topological defects from symmetry breaking. Int. J. Mod. Phys. A 29, 1430018 (2014).

[6] Doan, M.L. and Gary, G., 2009. Rock pulverization at high strain rate near the San Andreas fault. Nature Geoscience, 2(10), pp.709-712.

[7] Dor, O., Ben-Zion, Y., Rockwell, T.K. and Brune, J., 2006. Pulverized rocks in the Mojave section of the San Andreas Fault Zone. Earth and Planetary Science Letters, 245(3), pp.642-654.

[8] Frew, D.J., Forrestal, M.J. and Chen, W., 2002. Pulse shaping techniques for testing brittle materials with a split Hopkinson pressure bar. Experimental mechanics, 42(1), pp.93-106.

[9] Ghaffari, H.O. and Young, R.P., 2012. Topological complexity of frictional interfaces: friction networks. Nonlinear Processes in Geophysics, 19, pp.215-225.

[10] Grady, D. E. & Kipp, M. E. in Fracture Mechanics of Rocks (ed. Atkinson, B. E.) (Academic, 1987).

[11] Grady, D.E., 2008. Fragment size distributions from the dynamic fragmentation of brittle solids. International Journal of Impact Engineering, 35(12), pp.1557-1562.

[12] Grady, D.E., 2010. Length scales and size distributions in dynamic fragmentation. International Journal of Fracture, 163(1), pp.85-99.

[13] Hakim, V. and Karma, A., 2009. Laws of crack motion and phase-field models of fracture. Journal of the Mechanics and Physics of Solids, 57(2), pp.342-368.

[14] Harrison, W.A., 2012. Electronic structure and the properties of solids: the physics of the chemical bond. Courier Corporation.

[15] Huang, S., Liu, H., & Xia, K. (2014). A dynamic ball compression test for understanding rock crushing. *Review of Scientific Instruments*, *85*(12), 123902.

[16] Johnson, K.L. and Johnson, K.L., 1987. Contact mechanics. Cambridge university press.

[17] Key, W.R. and Schultz, R.A., 2011. Fault formation in porous sedimentary rocks at high strain rates: First results from the Upheaval Dome impact structure, Utah, USA. Geological Society of America Bulletin, 123(5-6), pp.1161-1170.

[18] Kibble, T.W., 1976. Topology of cosmic domains and strings. Journal of Physics A: Mathematical and General, 9(8), p.1387.

[19] Kittel, C., 1966. Introduction to solid state (Vol. 162). John Wiley & Sons.

[20] Kuramoto, Y.: Chemical Oscillations, Waves, and Turbulence, Springer-Verlag, Berlin, 1984.

[21] Laguna, P. & Zurek, W. H. Density of kinks after a quench: When symmetry breaks, how big are the pieces? Phys. Rev. Lett. 78, 2519 (1997).

[22] Lyakhovsky, V., Ben-Zion, Y., Ilchev, A. and Mendecki, A., 2016. Dynamic rupture in a damage-breakage rheology model. Geophysical Journal International, 206(2), pp.1126-1143.

[23] Lyakhovsky, V. and Ben-Zion, Y., 2014. Damage–breakage rheology model and solid-granular transition near brittle instability. Journal of the Mechanics and Physics of Solids, 64, pp.184-197.

[24] Mitchell, T.M., Ben-Zion, Y. and Shimamoto, T., 2011. Pulverized fault rocks and damage asymmetry along the Arima-Takatsuki Tectonic Line, Japan. Earth and Planetary Science Letters, 308(3), pp.284-297.

[25] Nielsen, S., E. Spagnuolo, S. A. F. Smith, Marie Violay, G. Di Toro, and A. Bistacchi. "Scaling in natural and laboratory earthquakes." *Geophysical Research Letters* 43, no. 4 (2016): 1504-1510.

[26] Olgaard, Brace, 1983. The microstructure of gouge from a mining-induced seismic shear zone. Int. J. Rock Mech. Min. Sci. Geomech. Abstr. 20 (1), 11e19.

[27] Reches, Z. & Dewers, T. A. Gouge formation by dynamic pulverization during earthquake rupture. Earth. Planet. Sci. Lett. 235, 361–374 (2005).

[28] Rempe, M., Mitchell, T., Renner, J., Nippress, S., Ben-Zion, Y. and Rockwell, T., 2013. Damage and seismic velocity structure of pulverized rocks near the San Andreas Fault. Journal of Geophysical Research: Solid Earth, 118(6), pp.2813-2831.

[29] Rowe, C.D. and Griffith, W.A., 2015. Do faults preserve a record of seismic slip: A second opinion. Journal of Structural Geology, 78, pp.1-26.

[30] Selvadurai, P.A. and Glaser, S.D., 2015. Novel monitoring techniques for characterizing frictional interfaces in the laboratory. Sensors, 15(5), pp.9791-9814.

[31] Truskinovsky, L. Fracture as a phase transition. Contemporary Research in the Mechanics and Mathematics of Materials 322–332 (1996).

[32] Wilson, B., Dewers, T., Reches, Z. & Brune, J. Particle size and energetics of gouge from earthquake rupture zones. Nature 434, 749–752

[33] Xia, K., Nasseri, M. H. B., Mohanty, B., Lu, F., Chen, R. & Luo, S. N. 2008 Effects of microstructures on dynamic compression of Barre granite. *Int. J. Rock Mech. Min. Sci.* **45**, 879–887. (doi:10.1016/j.ijrmms.2007.09.013)

[34] Xu, M.M., Huang, G.Y., Feng, S.S., McShane, G.J. and Stronge, W.J., 2016. Static and Dynamic Properties of Semi-Crystalline Polyethylene. Polymers, 8(4), p.77.

[35] Yuan, F., Prakash, V. and Tullis, T., 2011. Origin of pulverized rocks during earthquake fault rupture. Journal of Geophysical Research: Solid Earth, 116(B6).

[36] Zhang, Q.B. and Zhao, J., 2014. A review of dynamic experimental techniques and mechanical behaviour of rock materials. Rock mechanics and rock engineering, 47(4), pp.1411-1478.

[37] Zhou, F., Molinari, J.F. and Ramesh, K.T., 2005. A cohesive model based fragmentation analysis: effects of strain rate and initial defects distribution. International Journal of Solids and Structures, 42(18), pp.5181-5207.

Supplementary Information

1-Estimation of Normal Components of Colliding Velocity Using Pre-Scale Pressure Films

In this section, we estimate the kinetic energy term. The approach is based on the maximum indentation of the pressure films due to colliding of the flying fragmented particles. We assume the characteristic size of the fragments $<\xi>$ as the diameter of the planner disks which covers the circumference of a circular profile for a given position along the longitudinal direction of the cylinder (Fig.S1).

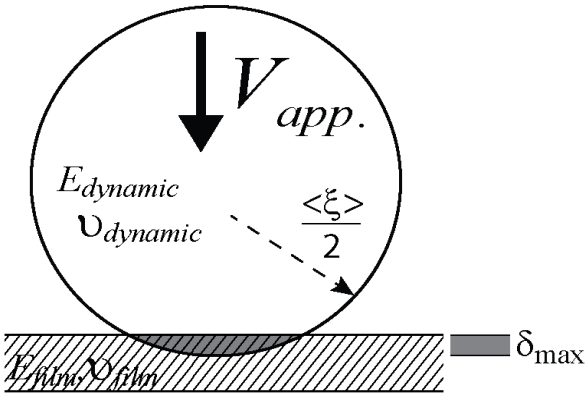

Figure S.1| A fragment with a circular shape collides with a pressure film. The maximum pressure is estimated based on maximum penetration depth and approaching velocity of particles.

Using the elastic *Hertzian* contact approach, we estimate the velocity of collision (velocity of approaching a fragment to the thin film). The first assumption is that the velocity vector is perpendicular to the thin film. The employed pressure films per each test estimate a local pressure (for a given pixel on the film). The maximum penetration depth on the film is given by:

$$\delta_{\max} = \left(\frac{15 m V_{app}^{2}}{16 <\xi>^{1/2} E^{*}}\right)^{2/5}, \qquad (1)$$

where m is the mean mass of each fragment , $V_{app.}$ is the colliding velocity and $\frac{1}{E^{*}} = \frac{1-\upsilon_{particle}^{2}}{E_{dynamic}} + \frac{1-\upsilon_{film}^{2}}{E_{film}}$ with $E_{dynamic}$ as the dynamic Young modulus for the dynamically loaded fragments and E_{film} is the Young's modulus of the film .

We assumed that the coupling of the film with capture ring is in a way that Young modulus of this combination is much higher than the approaching fragments. To estimate the maximum force, we calculate the overlap area between the infinitely curved film (1/R approaches zero, i.e., flat) and the penetrated particle in a depth of $\delta_{\max}$. The indentation area is given by:

$$S_{indent} = \frac{<\xi>^2}{4}[\cos^{-1}(1-\frac{2\delta_{\max}}{<\xi>})] - \frac{<\xi>}{2}(\delta_{\max} - \frac{<\xi>}{2})\sin[\cos^{-1}(1-\frac{2\delta_{\max}}{<\xi>})] \qquad (2)$$

Now we can estimate the maximum force using the recorded pressures :

$$F^{i}_{\max} = p_i S_{indent} = K\delta^{3/2}_{\max} \qquad (3)$$

with $K = \frac{4}{3}<\xi>^{1/2} E^*$ and S_{indent} is a function of $\delta_{\max}$. Using $\cos^{-1}(\square) \approx \frac{\pi}{2} - (\square + (\frac{1}{2})\frac{\square^3}{3})$, substituting (2) in (3) and knowing that $\frac{<\xi>}{2K}$ $\square$ 1 , we reach:

$$p(r,\theta) \approx \frac{4K\delta(r,\theta)^{\frac{3}{2}}}{(\frac{2\delta(r,\theta)}{<\xi>} + \frac{\pi}{2} - 1)<\xi>^2}, \qquad (4)$$

Therefore the estimate $\delta_{\max}$ in combination with (1) yields the maximum colliding velocity for a given element on the pressure film. A simplified form of (1) and (4) reads:

$$V_{app} \propto p(r,\theta)^{\beta} \; ; \; \beta = 1.2 \qquad (5)$$

Furthermore, the mean characteristic length of the fragments is controlled with the stress-pulse time-scale characteristic (i.e., input signal rate) which is given generally by a power law relation as follows [e.g., Grady, 1982]:

$$<\xi> \propto (\dot{\varepsilon})^{-b} \qquad (6)$$

in which $\dot{\varepsilon}$ is the rate of stress-pulse and $b>0$ is a constant exponent . From Eqs (1),(4-6) ,we reach to :

$$p(r,\theta) \propto (\dot{\varepsilon})^{\frac{3b}{5}} V^{\frac{1}{\beta}}_{app}(r,\theta) \qquad (7)$$

which indicates that the pressure-film patterns are scaled with the stress-pulse characteristics (as the external source) and the rate of exerted fragments.

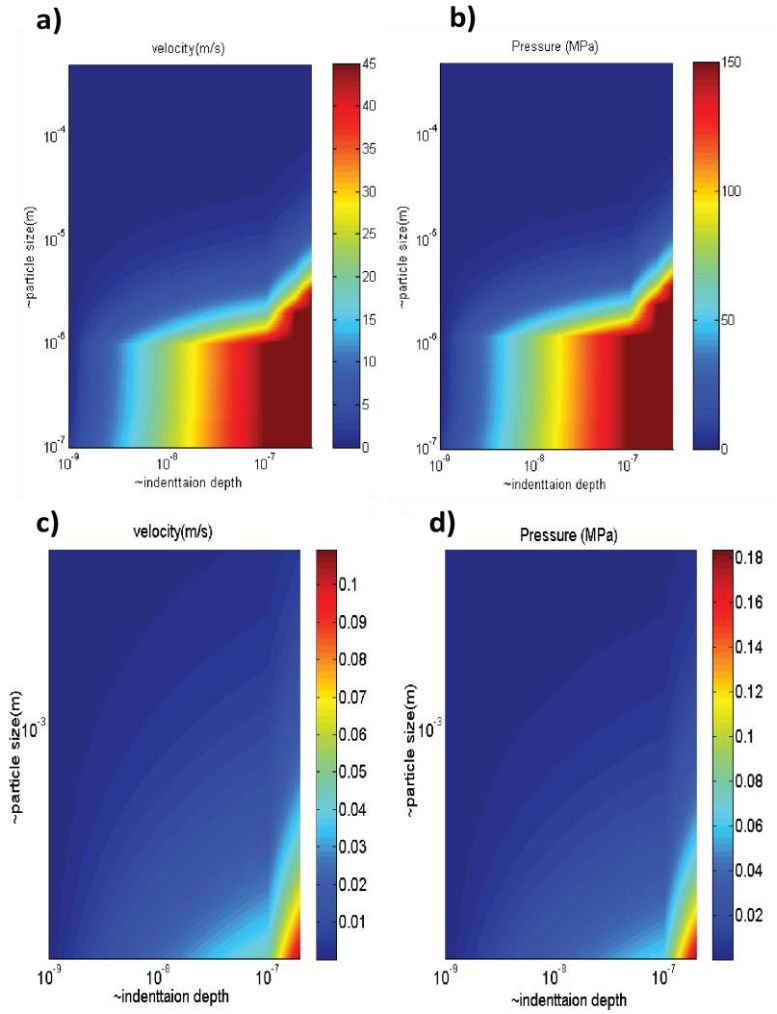

Figure S.2| Analytical calculations to explore range of pressure versus indentation depth and particle size. Indentation depth unit is in meter.

2-Calibrating prescale pressure films under dynamic loading

Pressure distributions due to impact of flying fragments are recorded on prescale pressure film that lines a steel capture ring surrounding the sample. Relevant dimensions are shown in Figure S3.

Color intensity recorded on the prescale film during each experiment is converted to a pressure value using an empirical color calibration curve. These curves differ markedly from the calibration curves provided by the manufacturer, which employ contact hold times of several seconds to minutes. In order to produce a color calibration curve valid for hold times of 10s to 100s of microseconds, we conducted a series of Split Hopkinson Pressure Bar Experiments in which the prescale film is sandwiched between two aluminum cylinders and loaded using a 6 inch striker bar. Loading pulses

were shaped by placing a copper disk between the incident and striker bar to ensure a constant strain rate during deformation, and amplitude of the incident pulses (controlling the peak axial pressure exerted on the aluminum cylinders and prescale film) were controlled by varying the muzzle velocity of the striker bar in each experiment. The result of each experiment is a circular region of red coloring, the darkness of which is related to the peak pressure (Fig. S4). The circular color intensity maps were converted to grayscale, and the mean value of the resulting grayscale color intensity distribution was plotted against recorded axial pressure to produce the non-linear color calibration curve. Note that error bars represent one standard deviation in the grayscale color maps. Using this calibration curve, we can convert each resulting pixel of color to a pressure value for visualization of resulting pressure patterns (Figure S4). Note that pressures below 10 MPa and above 150 MPa are omitted from analysis.

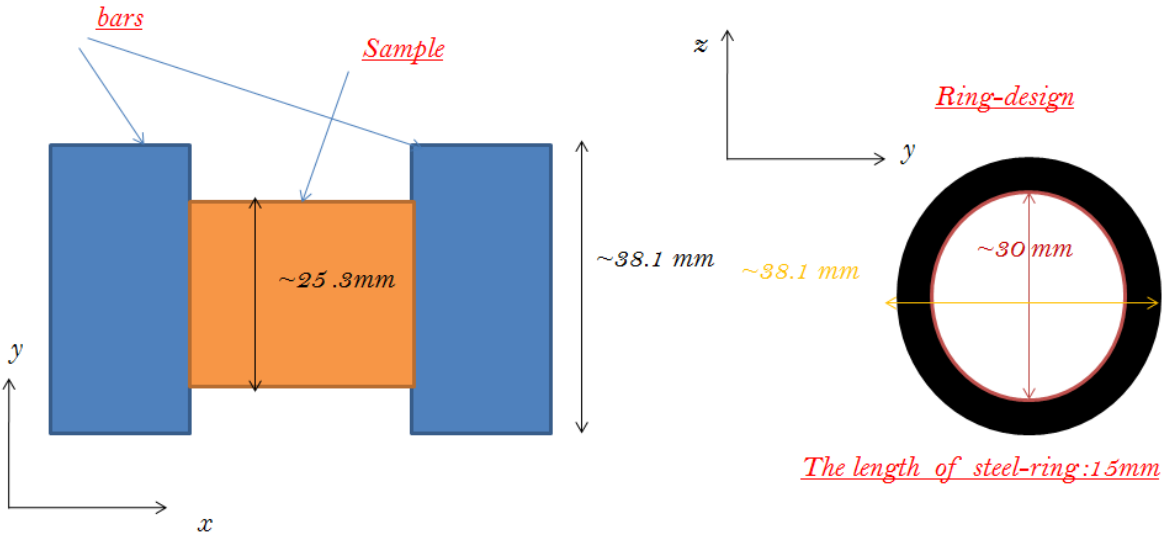

Figure S.3 The sample and the capture ring dimensions

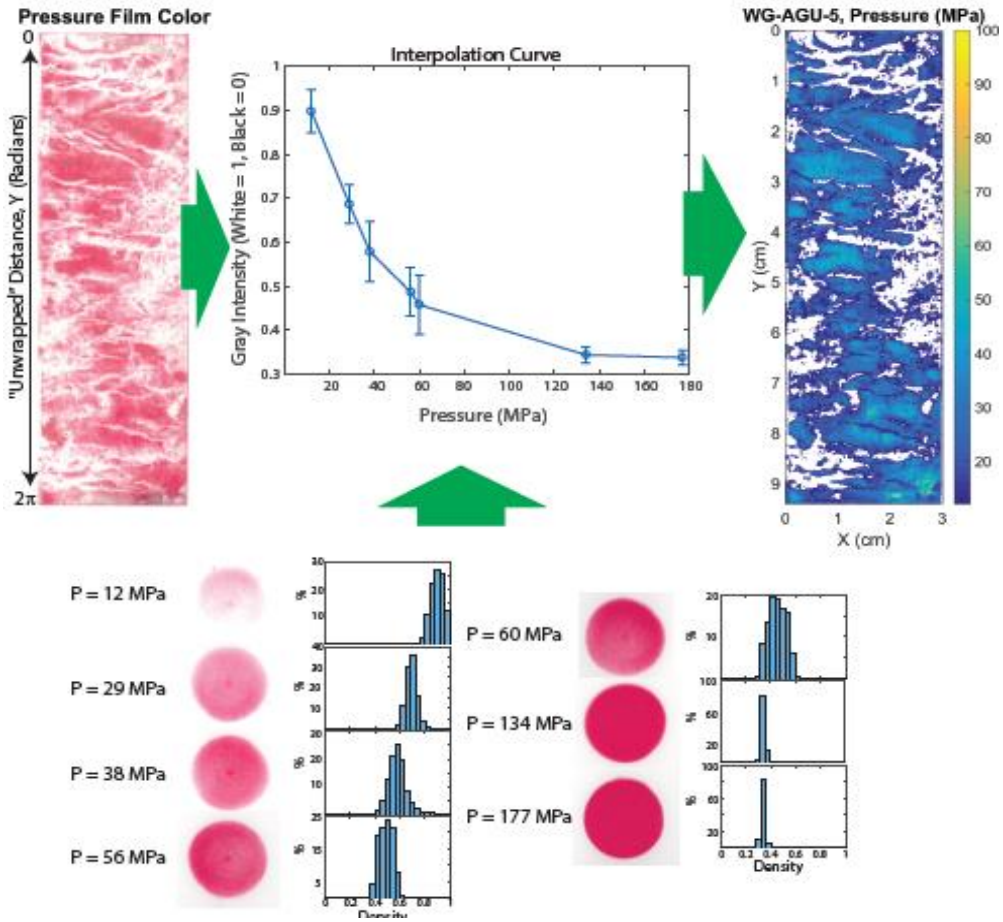

Figure S.4. Procedure of calibration of thin-pressure films (converting the color coded patterns into imprinted maximum pressures on the films).

699
700

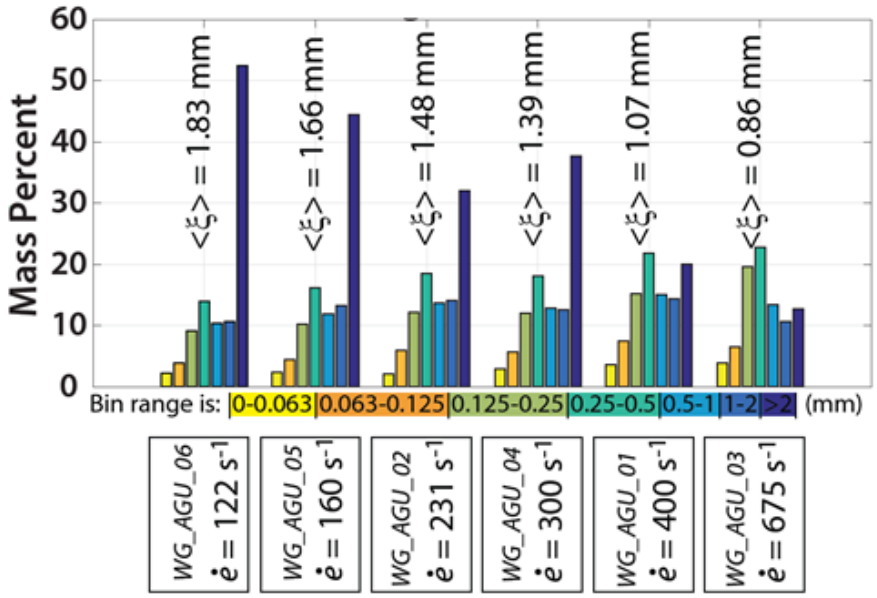

701

702 **Figure S.5. Particle size distribution for all produced particles**

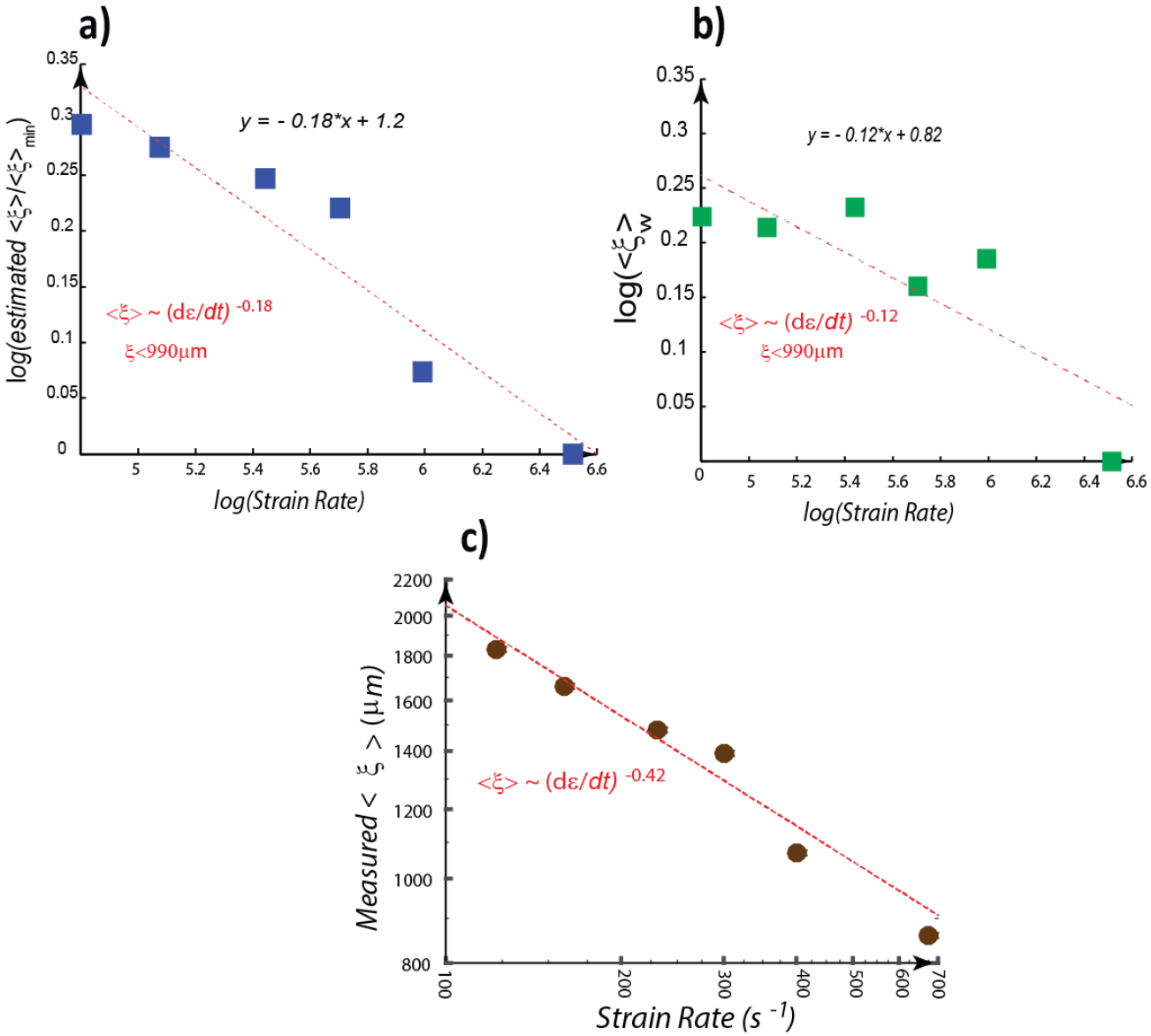

Figure S.6. Comparing b-values in calculated, modified and measured particles versus strain rates. **(a)** shows the log-log plot of normalized calculated fragments smaller than 990μm . All fragments are normalized to the smallest mean fragment size (highest strain rate) which was 432μm .This value corresponds to 0 in vertical axis. The b-value $<\xi>\sim(\frac{d\varepsilon}{dt})^{-b}$ is 0.18 . (b) Repeating the same procedure for the (weighted) measure particles with omitting particles larger than 990μm ,we get the b≈0.12. (c) The measurement for b for all particles yields b≈0.42.

3-Zero-kinetic energy modes of pre-scale pressure film

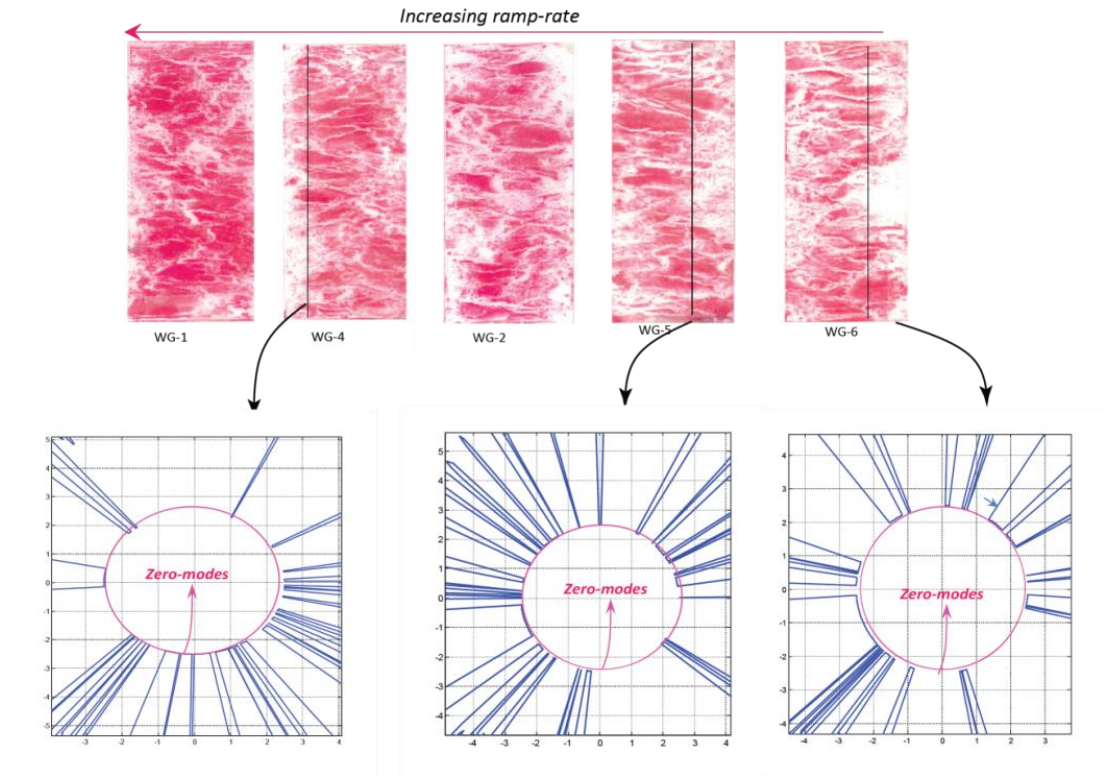

Figure S.7 Zero-energy modes for selected profiles. The red-circle is a reference to velocity vectors with zero-components.

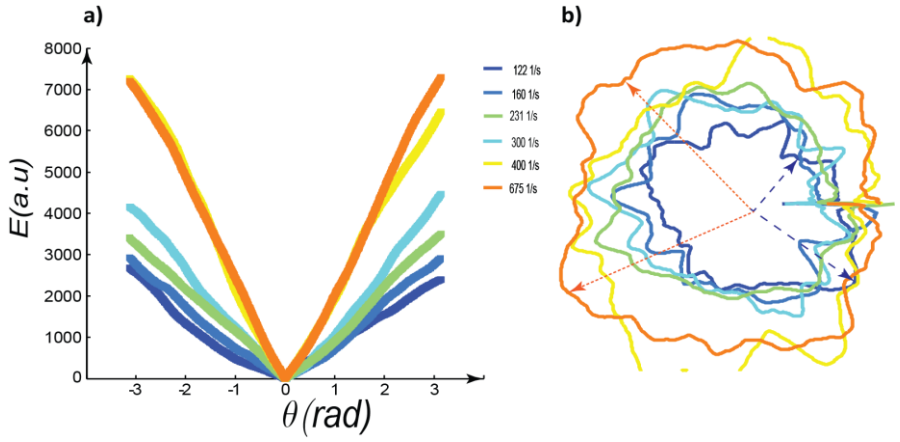

Figure S.8 (a) Energy spectrum for 6 different stress ramps averaged all over circumferential profiles (rings). **(b)** the mean velocity profiles smoothed with windows length of 20 units of pixels. The dotted arrows are the minimum and maximum directions of the velocity field.

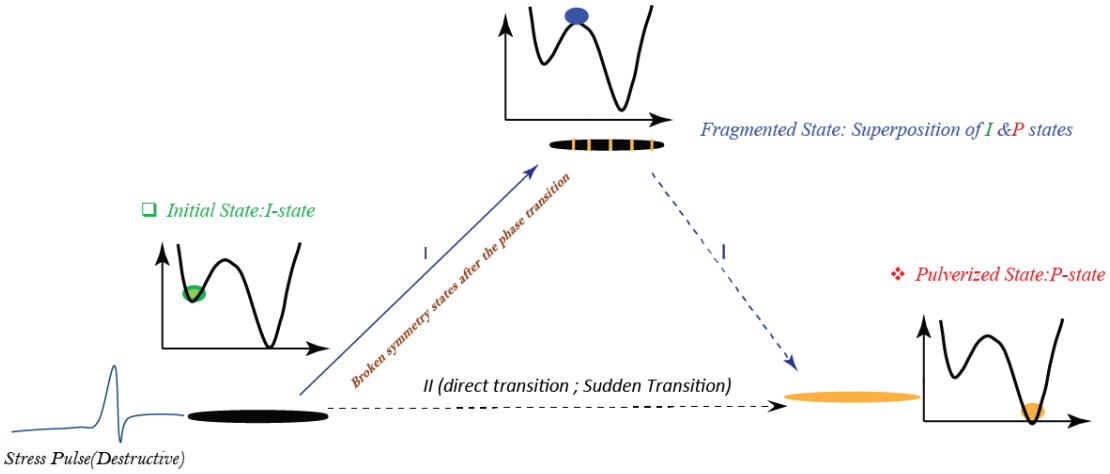

Figure S.9| Phase-transition from Intact state to pure pulverized state. We assumed the system moves on a rigid energy landscape. In reality the energy landscape is not rigid.

Supersonic Localized Excitations Mediate Microscopic Dynamic Failure

Authors: H.O. Ghaffari [1]*, M. Pec[1],W.A.Griffith[2]

Affiliations:

[1] Department of Earth, Atmospheric and Planetary Sciences, Massachusetts Institute of Technology, Cambridge, Massachusetts, USA

[2] School of Earth Sciences, Ohio State University, Columbus, Ohio, USA.

*Correspondence to: hoghaff@mit.edu

Abstract: A moving rupture front activates a fault patch by increasing stress above a threshold strength level. Subsequent failure yields fast slip and release of stored energy in the rock where a fraction of the released energy is radiated as seismic waves carrying information about the earthquake source. While this simplified model is widely accepted, the detailed evolution from the onset of dynamic failure to eventual re-equilibration is still poorly understood. Here, by measuring the dynamic stress fields near microscopic defects, we demonstrate that the stress history is mediated by formation and interaction of local excitations, or solitons which include collective movement of hundreds of atoms. Tracking of soliton motion unravels their extreme accelerations and short term supersonic propagation velocity which occur in transition to the fast weakening phase. Our results demonstrate a new microscopic quickening mechanism of the brittle failure process and open new horizons for understanding the complexity of earthquake sources.

MAIN TEXT

Introduction

The process of fracturing or splitting of many body systems, including solid materials, is accompanied by excitations, interactions and recombination of many quasiparticles as well as formation of defects, and thus represents an extremely challenging problem (11-15). It has been suggested that the general process of splitting matter evolves over at least two main time scales due to distinct fast and slow relaxation processes (8, 15-18). The fast relaxation (i.e., weakening phase) is accompanied by a dramatic change in the initial state of the system (2-5, 8, 17-18) and is usually followed by an intermediate state which is still out of equilibrium but forms a prelude to asymptotic relaxation to an equilibrium state (8,17). Here, we shed light on the processes occurring in the course of fast relaxation during dynamic failure of brittle solids.

We indented suspended thin sheets of single crystal mica and recorded the emitted ultrasound signals (high frequency analogues to seismic waves (6, 18)) using an array of 8 to 16 ultrasound sensors arranged in a ring around the indentation site (Fig.1- see Methods section). The simple geometry of the experiments allows us to unravel details of dynamic stress history of the laboratory earthquake sources in unprecedented detail. During an indentation test of the mica sheet, we were able to record tens of ultrasound excitations well known as acoustic emissions (AEs) with different excitation levels of source energy. In Fig.1b, we show waves from a single excitation parallel to the [001] direction of a muscovite mica specimen.

Results

To analyze the array of recorded AE signals, we map the ring-like structure of sensors to pseudo-spins (16-17, 19). We use a thresholded measure of each node's activity (measured in mV) to construct a dynamic "lattice" system of nodes that evolve throughout the recorded time series based on the behavior of the entire system (see Methods section for details). The constructed virtual lattice is characterized by the average of all nodes' degree (<k> - or mean coordinate number) and evolution of the lattice topology allows us to study the complexity of the excitation sources. The degree k_i of the i^{th} node at a given time represents the number of connected links to the node where "links" are established based on a similarity metric, therefore representing the intensity of spatial correlation

between the node and all other nodes (17, 20-21). Calibration of <k(t)> with pure impulsive compressive and shear sources indicates that the evolution of this parameter may be viewed as mean dynamic stress change (Methods part-Fig.S1-2). To visualize the evolution of the system, we map the spatial evolution of the degree k_i of the i^{th} node (Fig.1d), using polar coordinates $(R_i, \theta_i)_{i=1,\ldots,Nodes}$ where $R_i = k_i$ and θ_i indicate the position of the node around the ring (we call this structure a *k-chain*-Fig.1e). We infer a state for each node by assigning $s_i = sign(\frac{\partial k_i}{\partial t})$ so that $s_i = \pm 1$. With this mapping, each node in a given time step acquires one of two states, either up (↑) or down (↓).

Evaluating the recorded acoustic excitations, we found distinct patterns of dynamic failure characterized mainly by four peculiar phases (Fig.1d): (I) First, stress increases over a short time period (1 – 3 μs), (II) followed by rapid weakening (≈ 8-15 μs). Rapid weakening is followed by two distinct relaxation phases: (III) a temporary quasi-steady state phase (7-12 μs) followed by a (IV) long-term relaxation phase (> 50 μs). Here, we focus on the first two phases. In phase I, the system is pulled from an equilibrium state to a state where all sites (pseudo-spins) polarize in the outward direction. This occurs in the rising part of <k(t)> in Fig.1d and is stable for ~200-500 ns. After this short stable phase, kinks form by flipping one or more pseudo-spins, which interpolate between two pure-states of the system: up (↑) and down (↓). The formation of kinks can be visualized by the onset of "folding" of the chain, and we use the general term "soliton" to describe moving kinks (Fig.1e). Solitons are non-periodic waves that can be well-described by step-like functions of the form $tanh(\theta - v_{soliton}t/w)$ where $v_{soliton}$ is the propagation velocity of a soliton with a width, w, and position, θ (24,25). From a physical point of view, a kink can be viewed as a local defect and such defects affect the dynamical stress history during failure. A soliton moves with velocity $v_{soliton}$ and perturbs the initial state of the system (Fig.2 , also see *supplementary movie*). Tracking individual solitons indicates that they can propagate as fast as $v_{soliton}$~38km/s much faster than the p-wave velocity in mica (~5km/s). This observation highlights the role of long range interactions and is predicted by analytical solutions of nonlinear field theories as well as numerical simulations of supersonic dislocations (22-24).

To further illuminate the evolution of moving solitons, including their interactions and resultant effects on the inferred dynamic stress field, we present the evolution of density profiles based on kinetic energy of the k-chain: $E = \frac{1}{2}\sum_{i=1}^{N} m_i (\frac{du_i}{dt})^2$ where $\frac{dk_i}{dt} \equiv \frac{du_i}{dt}$ as the rate of normal displacement, N is the number of sites, and we assume a non-dimensional mass $m_i = 1$. We map the angular direction along a k-chain on to a vector $\mathbf{k}$ with fixed magnitude and direction Θ. Therefore, a system with N elements is characterized by $\mathbf{k}$ vectors and the energy E is defined in $\mathbf{k}$-space ($E(\mathbf{k})$). To characterize the energy distribution in $\mathbf{k}$-space (pseudo-momentum space), we use the concept of density of states in a 1-d chain as (25): $D(E) \propto \frac{1}{2\pi \left| \frac{dE}{d\theta} \right|}$ where $\theta = \frac{n\pi}{Na}$ and $n=1,\ldots,N$ (a is the lattice space). Therefore, the boundaries of the first Brillouin zone of a 1d k-chain lies at $\theta = \pm\pi$. Figure 2a shows an example of anisotropic evolution of a k-chain in $0 \le \theta \le \pi$ at the onset of a soliton-antisoliton pair formation. Approaching nucleation of the soliton, the instant energy of the chain monotonically decreases and eventually the onset of a soliton pair is visible in the density profile (Fig.2b). The nucleation points correspond to points with divergences in the density of states (in analogy with *Van Hove singularities-VHS* (26)) and splitting of VHS coincides with soliton-antisoliton propagation. In Fig.2.c, we show the nucleation, propagation and interaction of solitons which occurs in the transition from phase I to phase II. During this transition, we clearly observe that two solitons merge into a single short-lived pulse (i.e., strong merger regime (27)-Fig.S6-8).

In the example shown, solitons can propagate as fast as ~14 km/s, much faster than the p-wave velocity in the mica. Local excitations faster than p-waves hence govern the details of the transition, and play the role of "carriers of information". The transition to the second phase corresponds to the onset of stress relaxation and a fast-slip regime; failure occurs in the course of this transition. Tracking of soliton fronts along k-chains unravels the attractive interactions of colliding solitons (Fig.2c-Fig.S6-8). This attractive interaction leads to an increase in the front velocity up to ~ 37 km/s in less than a fraction of a micro-second implying an extreme local acceleration up to ~10^{11}m/s^2, five orders of magnitude higher than reported in laboratory stick-slip experiments (2, 5) suggesting a natural quickening mechanism of fast-slip phase in micro-failures (Fig.S3). The attractive interaction may occur due to the nonlocal nonlinear nature of the medium in which the response at a certain site is transferred to the surrounding regions and induces a spatially long-range response of the medium (28). The lifetime of fast fronts (maximum ~ 800 ns) is shorter than the lifetime of slower fronts (maximum a few micro-seconds). Due to annihilation of the solitons, the evolution path of the system after

crossing the peak of <k> is reversed and the system approaches another pure state in which all sites point inward (i.e., ↓↓ ...↓ - Fig.2c). Therefore, for a while the system experiences a state without any solitons. It has been proposed (25, 29, 30) that accelerated solitons or solitons with velocities approaching the maximum allowed velocity in the given structure (in analogy to the effective speed of light) exhibit relativistic features. In Figure 3 we show the trajectory of a soliton in transition from phase I to II where a sudden jump in the front velocity of up to 15 times the initial velocity is observed. After this sudden acceleration, the velocity of the soliton approaches ~25 km/s and its width *w* shrinks by ~30% of the initial length. This is a clear observation of Lorentz contraction which hints at the existence of relativistic features in the splitting process of a solid body.

Discussion

Our results provide new fundamental insights into how the strength of material evolves throughout microscopic dynamic failure. Unprecedented tracking of single soliton motion unraveled their extreme accelerations with supersonic to hypersonic velocities which occur in the course of the fast weakening phase - the most critical phase of any dynamic failure. Sudden extreme accelerations of soliton pulses should involve significant energy consumption, hence modifying the energy partitioning of microscopic failure as well as earthquakes. Motivated by our results, we suggest that observed accelerations of approximately 11 orders of magnitude and hypersonic stress pulse velocities provide extreme environment for destroying the matter and could cause the co-occurrence of emitted electrons and photons in course of dynamic failures and earthquakes (11-13).

References and Notes:

[1] Heaton, T. H. Evidence for and implications of self-healing pulses of slip in earthquake rupture. Phys. Earth Planet. Inter. 64, 1 (1990).

[2] Ohnaka, M. and Yamashita, T. A cohesive zone model for dynamic shear faulting based on experimentally inferred constitutive relation and strong motion source parameters. J. Geophys. Res. 94, 4089 (1989).

[3] Kanamori, H. and Rivera, L. in Earthquakes: Radiated Energy and the Physics of Faulting, R. E. Abercrombie, A. McGarr, G. Di Toro, H. Kanamori, Eds. (AGU, Washington, DC, 2006), pp. 3–13.

[4] Scholz, C. H. The Mechanics of Earthquakes and Faulting 2nd edn, 496 (Cambridge Univ. Press, 2002).

[5] Chang, J. C., Lockner, D. A. & Reches, Z. Rapid acceleration leads to rapid weakening in earthquake-like laboratory experiments. Science 338, 101–105 (2012).

[6] Benson, P. M., Vinciguerra, S., Meredith, P. G. & Young, R. P. Laboratory simulation of volcano seismicity. Science 322(5899), 249–252 (2008).

[7] Tinti, E., Spudich, P. & Cocco, M. Earthquake fracture energy inferred from kinematic rupture models on extended faults. J. Geophys. Res. 110, B12303 (2005).

[8] Ben-David, O., Rubinstein, S. & Fineberg, J. Slip-Stick: The evolution of frictional strength. Nature 463, 76 (2010).

[9] Buehler, M. J. & Gao, H. Dynamical fracture instabilities due to local hyperelasticity at crack tips. *Nature* **439**, 307–310 (2006)

[10] Livne, A., Bouchbinder, E., Svetlizky, I. & Fineberg, J. The near-tip fields of fast cracks. Science 327, 1359–1363 (2010).

[11] Dickinson, J.T., Donaldson, E.E. and Park, M.K., The emission of electrons and positive ions from fracture of materials. Journal of Materials Science, 16(10), pp.2897-2908 (1981).

[12] Theofanis, P.L., Jaramillo-Botero, A., Goddard III, W.A. and Xiao, H. Nonadiabatic study of dynamic electronic effects during brittle fracture of silicon. Physical review letters, 108(4), p.045501(2012).

[13] Enomoto, Y. and Hashimoto, H. Emission of charged particles from indentation fracture of rocks. Nature, 346(6285), pp.641-643 (1990).

[14] Kermode, J. R. et al. Low-speed fracture instabilities in a brittle crystal. Nature 455, 1224–1227 (2008).

[15] Gring, M. et al. Relaxation and prethermalization in an isolated quantum system. Science 337, 1318–1322 (2012).

[16] Ghaffari, H. O., & Young, R. P. Acoustic-friction networks and the evolution of precursor rupture fronts in laboratory earthquakes. Scientific Reports, 3. (2013).

[17] Ghaffari, H. O., W. A. Griffth, P. M. Benson, K. Xia, and R. P. Young. Observation of the Kibble–Zurek mechanism in microscopic acoustic crackling noises. Scientific Reports 6 (2016).

[18] Mclaskey, G. C., and Yamashita, F. Slow and fast ruptures on a laboratory fault controlled by loading characteristics. J. Geophys. Res (2017).

[19] He, C. et al. Acoustic topological insulator and robust one-way sound transport. Nat. Phys. 12, 1124–1129 (2016).

[20] Ghaffari, H. O., Thompson, B. D. & Young, R. P. Complex networks and waveforms from acoustic emissions in laboratory earthquakes. Nonlinear Processes Geophys. 21, 4 (2014).

[21] Newman, M. E. J. Networks: *An Introduction* (Oxford University Press, 2010).

[22] Bishop, A. R., and Lomdahl. P. S. Nonlinear dynamics in driven, damped sine-Gordon systems. Physica D: Nonlinear Phenomena. 18, 54-66 (1986).

[23] Peyrard, M., Pnevmatikos, S.& Flytzanis, N. Discreteness effects on non-topological kink soliton dynamics in nonlinear lattices. Physica D: Nonlinear Phenomena, 19(2), pp.268-281(1986).

[24] Gumbsch, P. & Gao, H. Dislocations faster than the speed of sound. Science 283, 965–968 (1999).

[25] Heeger, A. J., Kivelson, S., Schrieffer, J. R. & Su, W. P. Solitons in conducting polymers. Rev. Mod. Phys. 60, 781–850 (1988)

[26] Van Hove, L. The occurrence of singularities in the elastic frequency distribution of a crystal. Phys. Rev. 89, 1189–1193 (1953)

[27] Khaykovich, L. & Malomed, B. A. Deviation from one dimensionality in stationary properties and collisional dynamics of matter-wave solitons. Phys. Rev. A 74, 023607 (2006).

[28] Snyder, A. W. & Mitchell, D. J. Accessible solitons. Science 276, 1538–1541 (1997).

[29] Kivshar Y. S. & Malomed B. A. Dynamics of solitons in nearly integrable systems. Rev. Mod. Phys. 61, 763–915 (1989).

[30] Fernandez, J.C., Goupil, M.J., Legrand, O. and Reinisch, G., Relativistic dynamics of sine-Gordon solitons trapped in confining potentials. Physical Review B, 34 (1986).

Materials and Methods

Experimental procedures:

We indented Muscovite Mica specimens (from Princeton Scientific Corp). The indentation of mica sheets was performed parallel to [001] direction. We first suspended a thin sheet of mica on a ring–like structure of ultrasound sensors and carefully glued on the sensors. Then, we mechanically exfoliated the mica by peeling sheets from the top of the specimen. We repeated this process 10 to 15 times to achieve a thin layer (~5-20 μm) of the mineral sheet suspended on the sensors. The central indentation was performed using a micro-indentation instrument (DUH-211). We used different loading scenarios of loading with loading rates of 3mN/s. Our focus here was on the recoded excitations during loading or creep stage of the tests. In order to detect ultrasound excitations, we utilized piezoelectric sensors with frequency bandwidth of the transducers of 0.1 to 2.5 MHz. In the primary set-up (Fig.1), we used 8 sensors, to confirm the results we also employed a second set-up with 16 sensors (Fig.S4). The acoustic (ultrasound) excitation signals are first pre-amplified at 60 dB, before being received and digitized.

Analysis of emitted ultrasound waves:

We map the recorded array acoustic emission (array time series for each event) to a mathematical graph. We use a well-established algorithm to construct the mathematical graphs from our reordered acoustic emissions with a fixed number of nodes [16-17,20]. The main steps of the algorithm are as follows: (1) The waveforms recorded at each acoustic sensor are normalized to the maximum value of the amplitude at that node. (2) Each time series is divided according to maximum segmentation, such that each segment includes only one data point. The amplitude of the *j*th segment from the *i*th time series ($1 \le i \le N$) is denoted by $u^{i,j}(t)$ (in units of mV). *N* is the number of nodes or acoustic sensors. We set the length of each segment as a unit with a resolution of 25ns. (3) $u^{i,j}(t)$ is compared with $u^{k,j}(t)$ to create links between the nodes. If $d(u^{i,j}(t),u^{k,j}(t)) \le \zeta$ (where ζ is the threshold level) we set $a_{ik}(j)=1$ otherwise $a_{ik}(j)=0$ where $a_{ik}(j)$ is the component of the connectivity matrix and $d(\square)=\|u^{i,j}(t)-u^{k,j}(t)\|$ is the employed *similarity metric*. With this metric, we simply compare the normalized amplitude of sensors in the given time-step. The employed norm in our algorithm is the absolute norm. (4) Threshold level (ζ): To select a threshold level, we use a method introduced in (20, 31) and references therein) that uses an adaptive threshold criterion to select ζ. The result of this algorithm is an adjacency matrix with components given by $a(x_i(t),x_k(t))=\Theta(\zeta-|u^{i,j}(t)-u^{k,j}(t)|)$. Here $\Theta(.)$ is the Heaviside function. The constructed lattice is characterized by the average of all nodes' degree (<k>), where the degree, k_i, is the number of links formed between each node *i* and all other nodes in the system. For each node we assign $s_i=sign(\frac{\partial k_i}{\partial t})$ and then $s_i=\pm 1$. With this mapping, each node in a given time step acquires one of the states ($\uparrow$ or $\downarrow$). We use a fixed number of pseudo-spins (*N=300 nodes*) with interpolating the connectivity matrix, resulting the lattice constant as *a=0.2386mm* . To confirm the results, we also used a second set-up with 16 transducers where we indented a similar Muscovite Mica on a substrate of Si wafer where the lattice parameter for N=300 nodes was *a=1.03mm.*

Relationship with *Fermi-Dirac* Distribution and *Buehler-Gao's* interpretation of interatomic force:

Here we provide a semi-theoretical proof of k-chains to measure strain or stress fields. To do this, we map the k-chains onto a free electron gas model and use *Buehler-Gao's* interpretation of interatomic force (hereafter B-G's model). To start we assume a configuration of a k-chain prior to onset of a local excitation. The clusters –or communities [16, 20]- of the similar sub-energies carry out the energy of the chain; hence we define a certain number of the main energy levels (*m*) and as a first order approximation, we consider non-interactive energy levels. Each energy level does include sub-level energies which through the links form a community; in non-interactive energy clusters the links are purely within main energy levels and do not extend to other energy levels ("*ideal gas*" analogy). We assign a kinetic energy to each level ε_i and abundance of the i^{th} state k_i which is proportional with the occupation number of the i^{th} level $\sum k_i$ and summation goes over *m*-main energy levels. The k_i is, then, number of within links which is established between sub-levels of i^{th} level. We use a probabilistic argument that probability of finding an energy level with a higher value declines exponentially proportional with the energy level. Furthermore, we can define a maximum kinetic energy μ as a reference point; this is the allowed maximum kinetic energy level (in analogy with Fermi level). The occupation number of i^{th} energy level is, therefore, given by Fermi-Dirac distribution [32]: $n_i = \frac{1}{e^{(\varepsilon_i-\mu)/T}}$ in which n_i is the occupation number of the i^{th} energy level, ε_i is the kinetic energy, μ is the internal chemical potential (at zero temperature, this is the maximum kinetic energy, i.e. Fermi energy), T is the absolute temperature k_B is the Boltzmann constant. Now, we relate the above argument to stress-strain curve (Force-distance). To this end, we use *Buehler-Gao's* interpretation of interatomic force versus atomic separation *r* which is given by (9): $F(r) = k(r - r_0)\left[1 - \frac{1}{e^{(r^2 - r_c^2)/\Xi}}\right]$ where the parameter r_0 refers to the nearest-neighbor spacing of atoms. Assuming that the spring constant *k* is fixed, the *F(r)* has two other free parameters, r_c and Ξ. The parameter r_c corresponds to the Fermi energy in the Fermi–Dirac function μ and denotes the critical separation for breaking of the atomic bonds. The parameter Ξ corresponds to the temperature in the Fermi–Dirac function and describes the amount of smoothing at the breaking point. The exact mapping can be achieved by $r \leftrightarrow \varepsilon, \Xi \leftrightarrow \frac{1}{\beta}, r_c \leftrightarrow \mu$ (9). Thus, the evolution of i^{th} energy level in a k-chain is related to interatomic separation as follows: $r_i = r_c - k_B T \log(\frac{\sum k_i}{k_i} - 1)$ which indicates that the growth of the energy levels are exponentially proportional with the interatomic separation and therefore cohesive stress (Fig.S.3). Interestingly, the later conclusion confirms our calibration results upon to the failure point in which a semi-logarithmic change of the strain is scaled with the variation of node's degree (Fig.S.2d). It is noteworthy that increasing effective temperature in B-G's model- thermal energy is Boltzmann's constant *k* multiplied by temperature *T*- is in direct connection with the smoothness of the stress-strain curve in vicinity of the failure point; increasing temperature yields smoother curvature in failure point. Knowing that the solitionc mode -including number of solitons and their interactions -significantly shapes the smoothness of the failure curve, therefore ,we assign the effective temperature to a measure of soliton state in <k>-t curves. This inference suggests that soliton can be used equally as measure of effective temperature.

Calibration of k-chains with mechanical impulsive sources:

To associate <k(t)> with a physical source parameter, we used recorded un-amplified AE signals from known sources of impulsive compressive and shear loads recorded on a ring-like array of ultrasound transducers (Fig.S1-2). To generate compressive stress (in the order of induced strain rate ~$10^1 s^{-1}$), we use spilt Hopkinson pressure bar apparatus where an impulsive stress pulse is generated by a cylindrical steel projectile (the striker bar). The flying striker bar impacts an incident bar of identical material and diameter (Fig.S2a). The source signal is transferred through the incident bar and impacts a second bar which we mounted with 6-array Piezo-electric transducers. Using Dynamic linear strain gauges and knowing that the apparatus generates compressive stresses, we can compare <k(t)> with the strain gauge records (i.e., strain and stress on the bar). Here the source has the shape of a Gaussian function with superimposed oscillations due to the resonance of the bar (Fig.S2 c). The calculated <k(t)> -phase I of the evolution-is compared with recorded strain (Fig.S2d), indicating that <k>-profiles capture main features of the stress change. To compare the

<k(t)> with shear sources, we used similar unamplified ultrasound transducers as well as dynamic strain gauges and an accelerometer while two halves of the saw-cut Westerly granite slide on each other (Fig.S1-(33-34)). We confirmed that the calculated <k(t)> represent dynamic stress change on the interface due to abrupt stress drop (stick-slip tests). Neither measured acceleration nor measured velocity represent the <k(t)>. The form of the <k(T)> profiles measured resemble slip within granite blocks (35-36) during propagation of rapid macro-rupture fronts .The fact the we could infer the stress field history with measures of correlations of near-field piezoelectric sensors activities indicates that dynamic long-range interactions between the vibrating atoms play a vital role in defining relaxation path of the exited system.

Acknowledgments: The Methods section contains additional material about sample preparation and characterization together with detailed descriptions of the employed algorithm to construct k-chains from ultrasound excitations and calibration measurements. The k-chain implementation using recorded ultrasound excitations is available upon request. The data that support the plots within this paper and other findings of this study are available from one of the corresponding authors (H.O.Ghaffari) upon request. Supplementary information accompanies this paper. Research was sponsored partly by the Army Research Laboratory under Grant Number (W911NF-14-1-0276). All authors contributed to the analysis the results and reviewed the manuscript. H.O.G wrote the manuscript. H.O.G and W.A.G designed the main tests and performed the calculations. W.A.G and M.P supervised the research and helped to analyze the results

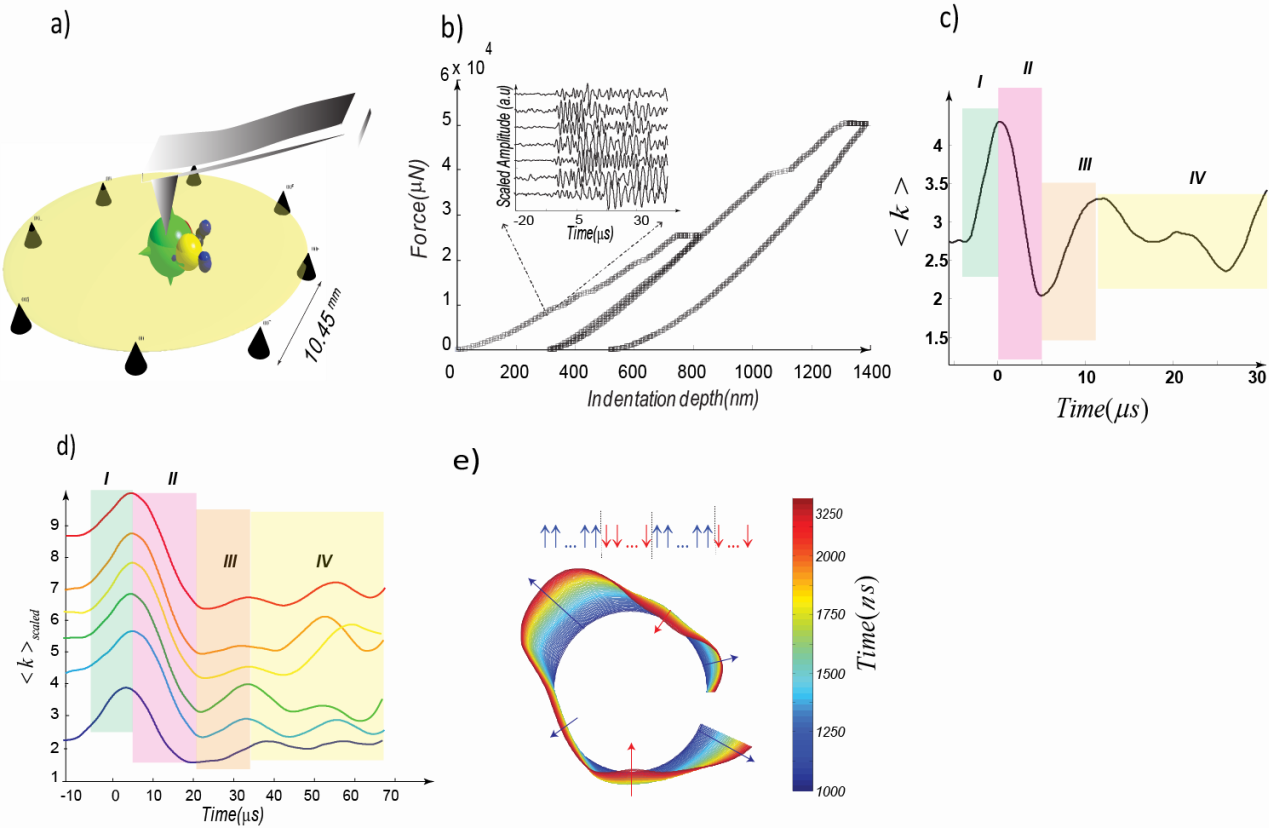

Fig. 1. **Acoustic-phonon excitations in indentation of suspended Mica-films (a)** Schematic representation of indentation. Thin Mica sheet is suspended over 8 piezoelectric transducers. The spheres correspond to locations where acoustic phonons are emitted as determined by a source location algorithm. **(b)** Two loading-unloading paths with clear pop-out events accompanied by ultrasound vibration of the receivers. Inset shows an array of recorded excitations during the loading stage. **(c)** Evolution of average of all nodes' degree <k> for waveforms shown in (b) showing four temporal stages of relaxation. In (**d**) we show 6 different acoustic events transformed to <k(t)>, where <k(t)> represents evolution of dynamic stress (see text). The system relaxes through four main phases. After initial rising phase (Phase I), a fast relaxation phase (phase II) is followed which stretches to a quasi-steady "re-strengthening" phase (III). Further relaxation occurs on longer

timescales (phase IV). **(e)** Accumulated k-chain patterns in ~1250ns time-interval in transition from phase I to phase II for the plot shown in (c).

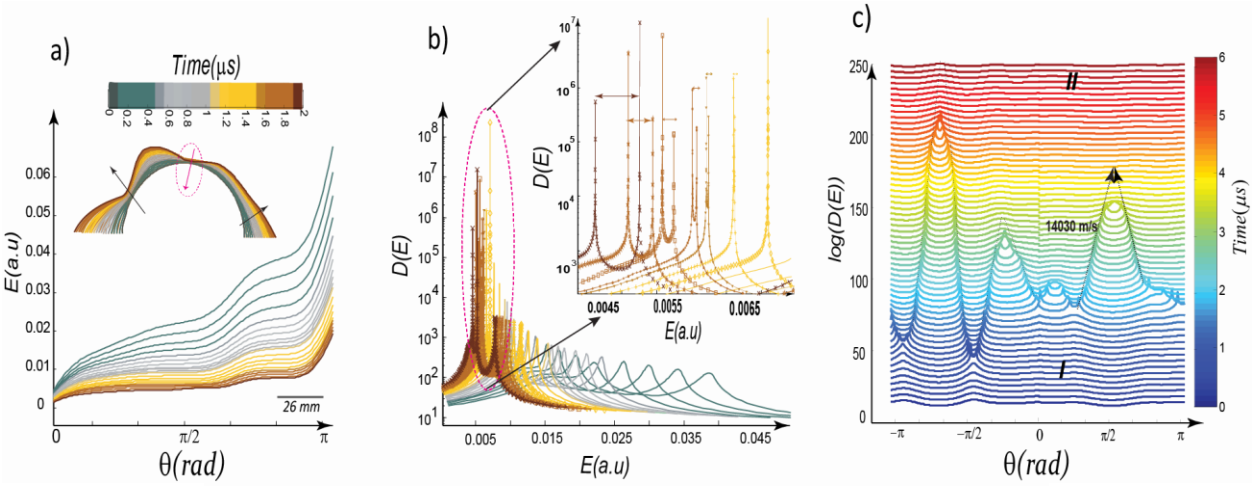

Fig. 2. Formatio in arbitrary units) as a function of d n decreases upon approaching nucl f the k-chain. (b) Singularity in der ows the splitting between the Van n-pairs. Here the shown pairs with e arrows show the distance of the sc occurring during transition of phase velocities relative to sound propagat and annihilation of fronts. The λ-s ee Supplementary Fig.S6-8). A clos s –deviation from linear trend highl ween 0μs to 6 μs in 0.1 μs increme

θ(rad)

Fig. 3. Lorentz contraction in an accelerated soliton. a,b) Velocity transition of a moving kink with velocity of ~1.6km/s to ~25 km/s in transition from phase I→II, leading to a fast acceleration of ~1011 ms-2. The color denotes the passage of time. The density profiles are in 0.1 μs increments and are shifted vertically for clarity. c) Normalized soliton profiles with similar color coding as (a). Inset: We fit a step-like tanh function to get the width of solitons. The Lorentz contraction is evident in the profiles as a decrease in the width of the profiles when the speed of propagation is increased. d) The width of the soliton shrinks up to ~30% when the relative propagation velocity increases ~15.5 times its initial velocity (also see Fig.S9).

Supplementary Materials:

Fig. S1. Shear source and k-chains: we report the measured dynamic shear stress evolutions recorded by (dynamic) strain gauge while two halves of the saw-cut Westerly granite slide on each other leading to macro-slips.

Fig. S2. Compressive Source and k-chains. We show calibration of the employed ultrasound transducers with known source and (dynamic) strain gauges using impulsive dynamic loading tests (generated by split Hopkinson Pressure bar). We also show Semi-logarithmic scale of<k> vs. strain during the rising phase of strain-time prior to effects of bar-resonance.

Fig. S3. Variation of interatomic separation versus a state of a site (k_i) and for different temperatures

Fig. S4. A second set-up of 16 PZT-array and indenting a brittle sample on a thick aluminum substrate

Fig. S5. High frequency components of an excited signal in our indentation test coincides with the fast-weakening phase in<k(t)>.

Fig. S6. Density profiles with ʌ-shaped collision signature in I→II

Fig. S7. A 3D representation of energy versus time-momentum space indicates

Fig. S8. ʌ-shaped collision of two solitons where the velocity 1500 m/s accelerates to 38000 m/s

Fig. S9. We show another example of squeezing a moving kink's width as it accelerates

Movies S1-S3

References (*31-36*)

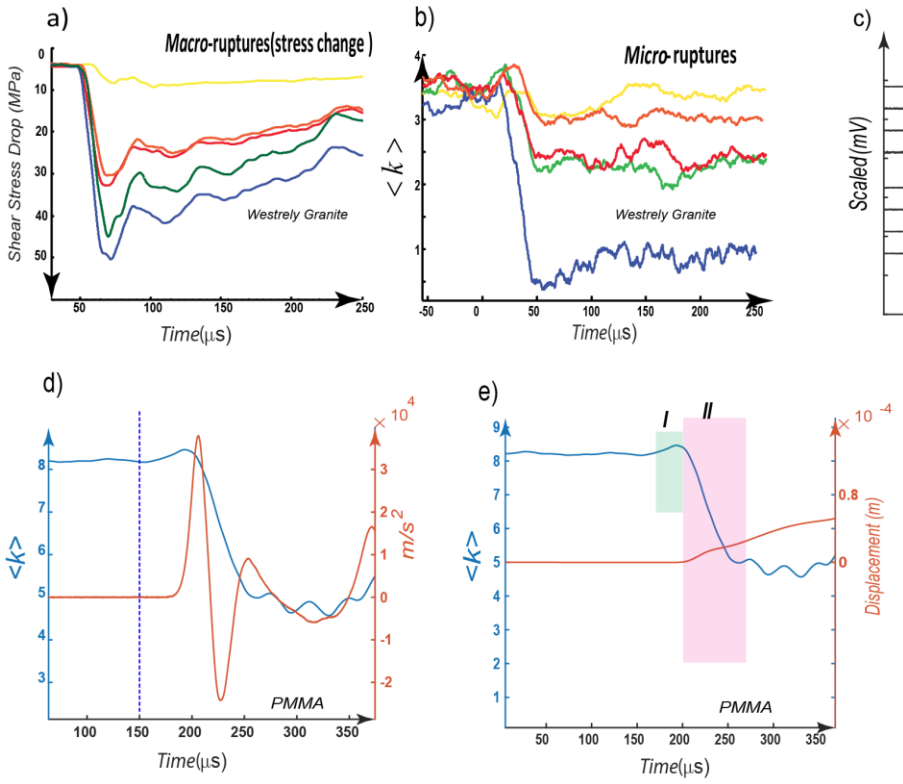

Figure.S1| Shear source and k-chains (a) the **measured dynamic shear stress** evolutions recorded by (dynamic) strain gauge while two halves of the saw-cut Westerly granite slide on each other leading to macro-slips. We show 5 stick-slip events. Wheatstone bridge strain gages are employed to record the dynamic (shear) stress change at 10MHz (the slope of the fault was 60 degree with horizon (32)) **(b)** The calculated <k(t)> based on micro-cracks prior to major stick-slip experiments based on recorded ultrasound excitations (33). **(c) The recoded unamplified waveforms** -after stacking- under

uniaxial stress while two halves of the PMMA-PMMA slide on each other. The blue dotted-line is the arrival of p-wave. **(d-e)** The calculated <k(t)> based on unamplified signals and super-imposed acceleration and displacements. The calculated <k(t)> represents dynamic stress change due to stick-slip and neither of measured acceleration or velocity represent the <k(t)>.

Figure. S2| Compressive Source and k-chains. Calibration of the employed ultrasound transducers with known source and (dynamic) strain gauges using impulsive dynamic loading tests (generated by split Hopkinson Pressure bar). (a) Here we show the response of the sensors to a controlled source tuned by the velocity of striker bar and pulse shaper. We used two dynamic strain gauges in incident and transmitted bar. We also used 5 unamplified piezo-electric transducers (PZTs) and one amplified (in 30dB) with the frequency bandwidth of the transducers from 0.2 to 1.3 MHz. The transducers were mounted on transmission bar in different positions. (b) Transmitted compressional signal (in red and negative sign of strain) superimposed on the recorded PZT signal. (c) Double plot of the recorded strain gauge and calculated <k> parameter. (d) Semi-logarithmic scale of<k> vs. strain during the rising phase of strain-time prior to effects of bar-resonance. (e) **Signature of damage signals superimposed on the recorded AEs under impulsive compressive -loading stress.** A disc of Westerly granite with thickness of 5 mm and diameter of 25 mm –sandwiched between two cylindrical leads- is used. In a case without sample, the PZT records the source pulse and resonance of bars where the sensors are mounted on it. The recorded signal in a case with a brittle sandwiched sample includes additional high vibrational modes which are not presented in the experiment without the sample. In (f),we magnified in the zone of high frequency interval for three recorded ultrasound emission signals with the duration of ~30μs.

Figure. S3| Variation of interatomic separation versus a state of a site (k_i) and for different k_BT with $k_B=1$. We have used $r_i = r_c - k_B T \log(\frac{m}{k_i} - 1)$ with $r_c = 1.5$ is the maximum allowed separation of the bonds (energy barrier in terms of thermal activation) and m is the number of energy-levels (communities or main evolutionary zones of the chain). In plotting this figure, we assumed a single energy level evolves while others are kept fixed.

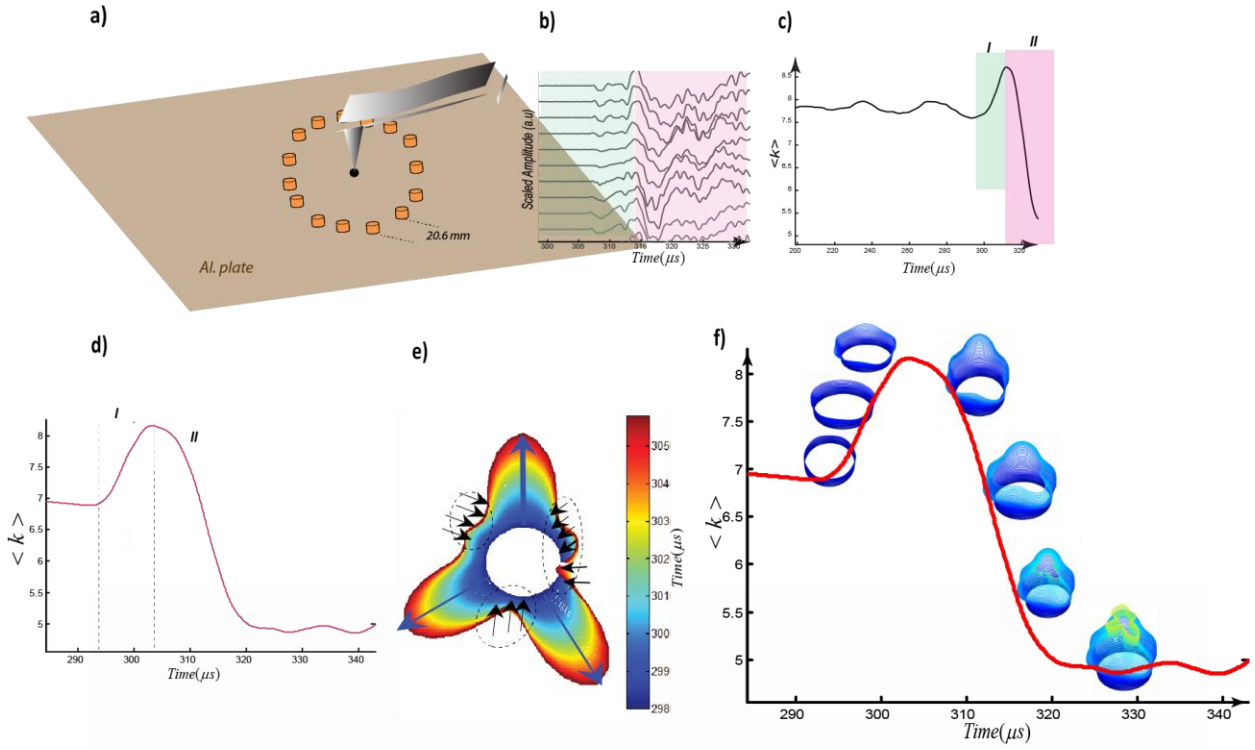

Figure **ate** (a) Record ath the sharp t ves are recorde o main phases arrival (d-e) th r_i=k_i . Based ase I is the con otropic strengt nferred from th trol the I-phase lso see *supple*

Time(μs)

Figure .S5| High frequency components of an excited signal in our indentation test are mapped onto fast-weakening phase in<k(t)>. Phase II corresponds with fast weakening phase and therefore <k(t)> represents dynamic weakening phase.

profiles moving of the elerated

Figure ergy of the cha s time- momen y carrv two op nt. The density

Figure. S8| (a,b) **ʌ-shaped collision** of two solitons where the velocity 1500 m/s accelerates to 38000 m/s . c) The trajectories of the moving solitons and fitting a linear line to obtain their velocity in the monitored time interval .

Figure. S9| Squeezing a moving kink's width as it accelerates a,b) Velocity transition of a moving kink with an average velocity of 1.6km/s to ~10 km/s in transition from phase I→II . The color denotes the passage of time. **c)** Normalized soliton profiles with similar color coding as (a). The Lorentz contraction is evident in the profiles as a decrease in the width of the profiles (dashed arrows) when the speed of propagation *v* is increased. We have shifted the profiles horizontally to show the effect of squeezing on the width of soliton. **d)** The width of the soliton shrinks up to ~45% when the relative propagation velocity increases ~6 times of its initial velocity.

[31] Ghaffari, H. O. & Young, R. P. Topological complexity of frictional interfaces: friction networks. *Nonlinear Processes Geophys.* 19, 215 (2012).
[32] Feynman, R. P. *Statistical Mechanics*: A Set of Lectures (Advanced Book Classics, 1998).
[33] Thompson, B. D., Young, R. P. & Lockner, D. A. Premonitory acoustic emissions and stick-slip in natural and smooth-faulted Westerly granite. *J Geophys Res*. 114, B02205J (2009).
[34] Ghaffari, H. O., Nasseri, M. H. B. & Young, R. P. Faulting of Rocks in a Three-Dimensional Stress Field by Micro-Anticracks. *Scientific report*, 4 (2014).
[35] Ohnaka, M. & Kuwahara, Y. Characteristic features of local breakdown near a crack-tip in the transition zone from nucleation to unstable rupture during stick-slip shear failure. *Tectonophysics* 175, 197–220 (1990).
[36]Okubo, P. G. & Dieterich, J. H. Effects of physical fault properties on frictional instabilities produced on simulated faults. *J. Geophys. Res.* 89, 5817–5827 (1984).